Systems/Circuits

Differential Effects of Astrocyte Manipulations on Learned Motor Behavior and Neuronal Ensembles in the Motor Cortex

Chloe Delepine,[1,2]* Jennifer Shih,[1,2]* Keji Li,[1,2]* ◉Pierre Gaudeaux,[1] and Mriganka Sur[1,2,3]

[1]The Picower Institute for Learning and Memory, Massachusetts Institute of Technology, Cambridge, Massachusetts 02139, [2]Department of Brain and Cognitive Sciences, Massachusetts Institute of Technology, Cambridge, Massachusetts 02139, and [3]Simons Center for the Social Brain, Massachusetts Institute of Technology, Cambridge, Massachusetts 02139

Although motor cortex is crucial for learning precise and reliable movements, whether and how astrocytes contribute to its plasticity and function during motor learning is unknown. Here, we report that astrocyte-specific manipulations in primary motor cortex (M1) during a lever push task alter motor learning and execution, as well as the underlying neuronal population coding. Mice that express decreased levels of the astrocyte glutamate transporter 1 (GLT1) show impaired and variable movement trajectories, whereas mice with increased astrocyte Gq signaling show decreased performance rates, delayed response times, and impaired trajectories. In both groups, which include male and female mice, M1 neurons have altered interneuronal correlations and impaired population representations of task parameters, including response time and movement trajectories. RNA sequencing further supports a role for M1 astrocytes in motor learning and shows changes in astrocytic expression of glutamate transporter genes, GABA transporter genes, and extracellular matrix protein genes in mice that have acquired this learned behavior. Thus, astrocytes coordinate M1 neuronal activity during motor learning, and our results suggest that this contributes to learned movement execution and dexterity through mechanisms that include regulation of neurotransmitter transport and calcium signaling.

Key words: astrocytes; *in vivo*; motor cortex; neuronal ensembles; RNAseq

Significance Statement

We demonstrate for the first time that in the M1 of mice, astrocyte function is critical for coordinating neuronal population activity during motor learning. We demonstrate that knockdown of astrocyte glutamate transporter GLT1 affects specific components of learning, such as smooth trajectory formation. Altering astrocyte calcium signaling by activation of Gq-DREADD upregulates GLT1 and affects other components of learning, such as response rates and reaction times as well as trajectory smoothness. In both manipulations, neuronal activity in motor cortex is dysregulated, but in different ways. Thus, astrocytes have a crucial role in motor learning via their influence on motor cortex neurons, and they do so by mechanisms that include regulation of glutamate transport and calcium signals.

Introduction

Astrocytes are the major glial cell type in the brain and have diverse properties (Khakh and Sofroniew, 2015; Chai et al., 2017; Verkhratsky and Nedergaard, 2018; Durkee and Araque, 2019), which modulate brain information processing from synaptic (Araque et al., 1999; Haydon, 2001) to network levels (Sasaki et al., 2014; Perea et al., 2014a; Mederos et al., 2019; Lines et al., 2020) to drive myriad behavioral outputs (Oliveira et al., 2015; Martin-Fernandez et al., 2017; Yu et al., 2018; Nagai et al., 2019). In particular, astrocytes modulate synaptic plasticity (Henneberger et al., 2010; Pannasch et al., 2011; Suzuki et al., 2011), leading to astrocyte-mediated neuronal circuit remodeling during memory formation and development (Adamsky et al., 2018; Hennes et al., 2020; Ackerman et al., 2021; Ribot et al., 2021; Zhou et al., 2021). However, astrocyte contributions to neuronal circuit function

during learned behavior remain largely unknown, although previous studies suggest they play a crucial role in acquiring memories and behaviors (Padmashri et al., 2015; Hösli et al., 2022). A handful of *in vivo* studies have directly probed the effects of astrocytes on individual neurons (Perea et al., 2014b) or neuronal populations (Poskanzer and Yuste, 2016; Lines et al., 2020), taking advantage of well-defined behavioral correlates to neuronal circuit function. Here, we investigated the role of cortical astrocytes *in vivo* during a motor learning task that relies on coordinated neuronal ensemble activity in the primary motor cortex (M1; Peters et al., 2014). During motor learning, both task acquisition (Nudo et al., 1996; Kawai et al., 2015) and performance (Dombeck et al., 2009; Harrison et al., 2012) are associated with neuronal and circuit remodeling. At the synaptic level, motor learning leads to structural and functional plasticity in M1 (Chen et al., 2015; Cichon and Gan, 2015; Gloor et al., 2015), suggesting that M1 astrocytes, by virtue of their role in synaptic plasticity, mediate neuronal population dynamics that drive acquisition of stereotyped movements and task performance.

Cortical astrocytes influence synaptic transmission via the glutamate transporter 1 (GLT1), which is expressed on the cell surface in the vicinity of synapses (Rothstein et al., 1994, 1996; Aida et al., 2015; Murphy-Royal et al., 2015). Astrocytes also express numerous G-protein-coupled receptors (GPCRs) that respond to, as well as modulate, neuronal activity via downstream second messenger systems (Porter and McCarthy, 1997; Agulhon et al., 2013; Kofuji and Araque, 2021). Both GLT1 function and Gq-GPCR pathway activation in astrocytes influence specific behaviors and underlying neuronal activity (John et al., 2012; Cao et al., 2013; Aida et al., 2015; Scofield et al., 2015; Chen et al., 2016; Kol et al., 2020; Iwai et al., 2021; Nagai et al., 2021). We therefore reasoned that altering astrocytic glutamate transporters or Gq signaling would reveal effects of astrocytes on neuronal encoding and learned motor behavior.

Here, we found that decreasing astrocytic glutamate clearance specifically in M1 prevented learning of a stereotypical motor trajectory while preserving response time and task success rate. Stimulating Gq signaling in M1 astrocytes also led to impaired learning of the movement trajectory, as well as impaired task performance. In M1 layer 2/3 neuronal populations, knockdown of astrocytic GLT1 increased the proportion of active neurons and decreased neuronal correlations during movement, whereas activation of astrocyte Gq signaling led to increased neuronal correlations. Decoding and encoding models showed changes in neuronal coding of task parameters following astrocyte manipulations, particularly in the representation of movement trajectories. We further confirmed that astrocytes contribute to mechanisms underlying motor learning by using RNA sequencing (RNAseq). In particular, we found significant enrichment of glutamate and GABA transporter transcripts in expert animals, suggesting a key role for neurotransmitter transport in M1 function during motor learning. Together, these findings demonstrate that astrocytes contribute to the functional and encoding capabilities of M1 layer 2/3 neuronal ensembles *in vivo* during motor learning and imply that astrocytes are critical for synaptic and circuit plasticity that drives learned behavior.

Materials and Methods

Experimental model
All experimental procedures performed on mice were approved by the Massachusetts Institute of Technology Animal Care and Use Committee and conformed to National Institutes of Health *Guidelines for the Care and Use of Laboratory Animals*. Adult mice (2–4 months old, C57BL/6J

background) were housed on 12 h light/dark cycle, group housed before surgery, and singly housed afterward. Male and female mice from the following mouse lines were purchased from The Jackson Laboratory: C57BL/6J wild-type (stock #000664), CaMKII;mTTA;GCAMP6s (mTTA;GCaMP6s: Ai94(TITL-GCaMP6s)-D;ROSA26-ZtTA (stock #024112), CaMKII-cre: B6.Cg-Tg(Camk2a-cre)T29-1Stl/J (stock #005359), GFAP;GCaMP5G (GFAP-cre: B6.Cg-Tg(Gfap-cre)77.6Mvs/2J (stock #024098), GCaMP5G, Polr2atm1(CAG-GCaMP5g,-tdTomato) Tvrd (stock #024477), Aldh1l1;GCaMP6f-Lck (Aldh1l1-cre: B6;FVB-Tg (Aldh1l1-cre)JD1884Htz/J (stock #023748), and GCaMP6f-Lck: C57BL/6N-Gt(ROSA)26Sortm1(CAG-GCaMP6f)Khakh/J (stock #029626). The GLT-1 flox line (Cui et al., 2014) was a gift from Kohichi Tanaka.

Stereotactic virus injection and craniotomy
Surgeries were performed aseptically under isoflurane anesthesia while maintaining body temperature at 37.5°C. Mice were given preemptive analgesia (slow release buprenex, 1 mg/kg, s.c.). Scalp hairs were removed with a depilatory cream, skin was sterilized with 70% ethanol and betadine, and a portion of the scalp was removed. Mice were head fixed in a stereotaxic frame (model 51725D, Stoelting). A round 3-mm-diameter craniotomy was performed over the left motor cortex (0.3 mm anterior and 1.5 mm lateral to bregma) and 200 nl of virus solution (titer of 10–12 virus molecules per ml) was injected 300 μm below the pial surface at 50 nl/min with a thin glass pipette and a stereotaxic injector (QSI 53311, Stoelting). Following each injection, the glass pipette was left in place for 15 additional min and was then slowly withdrawn to avoid virus backflow. The following viruses were used: adeno-associated virus (AAV)8-GFAP-hM3D(Gq)-mCherry (viral titer, 7E12 vg/ml; University of North Carolina Vector Core), AAV5.GFAP.Cre.WPRE.hGH (viral titer, 2.2E13 vg/ml; Penn ID AV-5-PV2408, Penn Vector Core), AAV1.Syn.GCaMP6s.WPRE.SV40 (viral titer, 1.9E13 vg/ml; Penn ID AV-1-PV2824, Penn Vector Core). Finally, a cranial window made of three round coverslips (CS-5R, 1 × 5 mm diameter; CS-3R, 2 × 3 mm diameter; Warner Instruments) glued together with UV-cured adhesive (catalog #NOA 61, Norland) was implanted over the craniotomy and sealed with dental cement (C&B Metabond, Parkell). For head fixation during the behavioral task and/or calcium imaging, a head plate was also affixed to the skull using dental cement (C&B Metabond, Parkell). Postoperative analgesic was provided (Meloxicam, 5 mg/kg, s.c.), and recovery was monitored for a minimum of 72 h after surgery. Animals recovered for at least 5 d before starting water restriction for behavioral experiments. After completion of experiments, we verified that targeting of the motor cortex region was successful by performing immunohistochemistry and fluorescence confocal imaging. Animals for which viral delivery was mistargeted or failed were excluded.

Behavioral testing
Water-restricted mice were head fixed and trained daily on a lever push task (Peters et al., 2014), modified as follows. The lever was built using a piezoelectric flexible force transducer (model LCL-113G, Omega Engineering) attached to a brass rod and could be reached easily by mice using their right paw. Another fixed brass rod was placed in front of the left paw. The voltage from the force transducer, which is proportional to the lever position, was continuously recorded. Lever press was defined as crossing a 1 mm threshold. A tone marked the beginning of a trial with a 5 s response period. A lever press past the threshold triggered a 6 μl water reward and the start of a 2.62 s reward time followed by an intertrial interval (ITI). Failure to press during the 5 s response period triggered a loud white noise and a 2.62 s timeout period followed by the ITI. Lever presses during the ITI were punished by delaying the start of the next trial until a full second of time passed without any lever movement. The system was controlled by MATLAB (MathWorks) using Psychtoolbox.

Clozapine-*N*-oxide administration
Clozapine-*N*-oxide (CNO; Enzo Life Sciences) was dissolved in saline injectable sterile solution (0.9% sodium chloride) and administered at a low concentration of 0.1 mg/kg (Kim et al., 2021; Vaidyanathan et al.,

2021). The CNO solution or saline control was injected intraperitoneally 30 min before each training session.

Two-photon microscopy
Mice were head fixed and GCaMP fluorescence imaging of the left motor cortex (0.3 mm anterior and 1.5 mm lateral to bregma) was performed through the cranial window, 2–6 weeks postvirus injection and after 3 d of habituation consisting of daily 10 min passive sessions. A Prairie Ultima IV two-photon microscopy system was used with a galvo-galvo scanning module (Bruker). A 910 nm wavelength excitation light was provided by a tunable Ti:Sapphire laser (Mai Tai eHP, Spectra-Physics) with dispersion compensation (DeepSee, Spectra-Physics), and the signal was collected by GaAsP photomultiplier tubes (Hamamatsu). Images were acquired using PrairieView acquisition software. A 16×/0.8 NA microscope objective (Nikon) was combined with 2× optical zoom to simultaneously image large numbers of neuronal somas, and image sequences were acquired at 5 Hz. A 521 × 236 pixel (274 × 274 μm) square FOV was imaged for 10 min during each expert training session of awake mice performing the lever push task (GCaMP6s) or passive imaging session in awake untrained mice (GCaMP5G).

Astrocyte activity image analysis
GCaMP5G fluorescence from the upper layers of the left motor cortex was acquired as described above in GFAP;GCaMP5G transgenic mice. After acquisition, time-lapse imaging sequences were corrected for *x* and *y* movement using the template-matching ImageJ plug-ins. Regions of interests (ROIs) were automatically identified using CaSCaDe (Agarwal et al., 2017). The baseline fluorescence F0 was calculated as the 25th percentile. DF/F0 = 100*(F – F0)/F0 was calculated where DF is the change in fluorescence, *F* is the ROI average fluorescence, and F0 the baseline fluorescence. DF/F0 peaks with values 3 SDs above the average DF/F0 were considered as calcium elevation events. The event amplitude was defined as its maximum DF/F0 value.

Neuronal activity image analysis
GCaMP6s fluorescence from the upper layers of the left motor cortex was acquired as described above in CaMKII;mTTA;GCAMP6s transgenic mice or, alternatively, wild-type mice injected with AAV1.Syn. GCaMP6s.WPRE.SV40. We used GCaMP6s for this study because of its higher signal-to-noise, which can better capture the motion information encoded in M1 neurons and especially, compared with GCaMP6f, its larger response amplitude, lower variability and thus greater single-spike detectability when used to infer spikes (Wei et al., 2020; Huang et al., 2021). After acquisition, time-lapse imaging sequences were corrected for *x* and *y* movement using template-matching ImageJ plug-ins. ROIs were automatically identified using Suite2P (Pachitariu et al., 2017) and then manually curated. In some cases, neuronal ROIs were manually selected. The fluorescence intensity in time for each ROI was then averaged. The DF/F0 = 100*(F – F0)/F0 was calculated, where *F* is the average signal and F0 the mode of the signal.

Average activity. Activity during movement or during ITI for each successful trial was defined, respectively, as the average DF/F0 across a 1 s epoch starting at movement onset or as the average DF/F0 across the final 1 s of the ITI (no movement). The average activity of a neuron was calculated as the average across all the successful trials of the activity during movement as defined above.

Movement-related active neurons. For each trial, a neuron was considered active if the maximum DF/F0 during movement was 2 SDs above the average DF/F0 during ITI. Percentage of movement related neurons was calculated for each trial and then averaged across all trials.

Neuron-to-neuron correlation. Neurons active for >10% of the trials were included in the analysis. For each neuron, activity data vectors during movement for all trials were concatenated into one vector. The pairwise distance correlation coefficient of two vectors was then computed to estimate neuron-to-neuron correlation.

Behavioral encoding model. We used encoding models to test and compare the accuracy of using different behavioral variables to predict the variability in neuronal activity during the lever push task trials in fully trained mice. We used a generalized linear model (GLM; Engelhard et al., 2019) modified as follows. Behavioral events, lever trajectory, and neuronal activity (DF/F0) during a 5 s period after the start of each correct trial were used. For each training session, data vectors for all trials were concatenated into one vector before fitting the model. We extracted seven basic features of the behavioral data in the model and spanned them temporally to facilitate a linear model. Three types of predictors were used, events, trial constants, and continuous variables. Two events, start of trial and reward, were included (reward was immediately given when the lever was pushed past the threshold). These events were converted into continuous variables with the same sampling rate as the neuronal activity, by convolving each with a seven-degrees-of-freedom regression spline basis set. Trial constants were single variables specific to a trial, including trial status (hit/miss, scored as 1 or 0, respectively) and response time as a number (time in s). These trial constants were converted to time series by convolving with a step function lasting the duration of the trial. Continuous variables included lever trajectory, lever speed, and lever motion (moving), each raised to a third degree polynomial. A special case was lever motion, which was an in-trial step function that was set to one before the movement onset and zero after onset. This predictor encoded whether a movement was occurring but did not differentiate how long the movement epoch was for each trial (details of predictor transformation were similar to those in Engelhard et al., 2019). The expanded predictors were scaled (*z*-scored) and fitted to a linear model for each neuron, regularized with an elastic net penalty. The accuracy of each GLM model was assessed by fivefold cross-validation (80% for training set, 20% for testing set). The encoding power R^2 was calculated for each prediction from the fitted model. We quantified the relative contribution of each behavioral variable to single-neuron activity by determining how the performance of the encoding model was reduced (decrease of R^2) when each variable was excluded from the predictor set of the model; the model was kept as is while setting the weights of the excluded feature to one. When excluding a variable, its derivative/expanded predictors were taken out as well.

Decoding analysis. To evaluate and compare the capacity of M1 neurons to encode the forelimb push trajectory, we tested a decoding model to predict the push trajectory from the neuronal population activity. The calcium activity (DF/F0) was deconvolved with an adaptive kernel to obtain an estimate of spiking activity (Vogelstein et al., 2010). We fitted a linear decoding model to the entire duration (600 s) of each training session, as well as to concatenated push trajectories alone, to predict the forelimb push trajectory from population spiking activity of the most informative 20 recorded M1 layer 2/3 neurons for each session. After evaluation of various M1 decoding models, we chose the support vector regression (SVR) model with radial basis function kernel for measuring the encoding information in M1 neurons for its stability (i.e., higher reliability with random split validation), which allowed us to compare neuron encoding capacities of populations from different animals in different groups. This model has two main hyperparameters— *γ*, the scaling parameter of the kernel, and C, the regularization parameter. They were optimized through grid search for the average prediction performance (as discussed below) across all cases in all treatment groups, and the same hyperparameters were used for all cases (*γ* = 1E-4, C = 12). For each session, a continuous segment of time making up 10% of the entire session starting at a randomized time point (typically, a 60 s segment in a 600 s training session) was used as the test period for model fitting, during which both behavioral and neuronal data were taken as the test dataset. The rest of the data was spliced together as the training set. To quantify the similarity between the model predicted trajectory and the actual trajectory, we used a modified version of the Non-Parametric Entropy Estimation Toolbox package (Ver Steeg and Galstyan, 2013). Briefly, we used a continuous estimation of mutual information by the average data point distance to the *k*th neighbor (usually used with *k* = 3). This mutual information between predicted trajectory and actual trajectory was used as the metric of encoding capacity of M1 neuron populations. This estimation of mutual information takes into account the dependence of the actual values within each variable, as opposed to simply comparing how the variances of each population correlate. Thus, this analysis is a generalization

of linear correlation measurements and considers information carried by nonlinear relationships between the two variables.

Immunohistochemistry

Mice were transcardially perfused with 0.9% saline followed by 4% paraformaldehyde in PBS. Coronal sections were cut to a thickness of 50 mm using a vibratome (VT1200S, Leica) and incubated for 1 h in blocking solution (0.1% Triton plus 3% BSA in PBS), then overnight in blocking solution with the primary antibody mouse anti S-100β subunit (1:1000; catalog #S2532, Sigma-Aldrich). Sections were washed and then incubated for 2 h in blocking solution with the secondary antibody goat anti-mouse 647 nm (1:500; catalog #A21235, Thermo Fischer Scientific). Sections were washed in PBS, then mounted on slides in hard set mounting medium containing 4,6-diamidino-2-phenylindole (VECTASHIELD, catalog #H-1500, Vector Laboratories). A confocal system (TCS SP8, Leica) was used to image the fluorescence of GCaMPs, mCherry, and S100β immunostaining, using 10×/0.40, 20×/0.75, or 63×/1.40 objectives (magnification/numerical aperture, Leica) and LAS X Acquisition Software (Leica).

Western blot

Mice were deeply anesthetized under isoflurane and decapitated for rapid brain extraction. Cortices were dissected (~4 mm^3 samples) in ice-cold 0.9% saline and meninges removed. Left and right M1 cortex biopsies were flash frozen and stored at $-8°C$. Frozen samples were later homogenized in ice-cold RIPA buffer (catalog #89901, Thermo Fisher Scientific) supplemented with phosphatase inhibitors (PhosSTOP, Roche) and protease inhibitors (cOmplete Mini EDTA-free, Roche) using a high-speed homogenizer (FastPrep-24 5G Instrument, MP Biomedicals). Pierce BCA Protein Assay Kit (Thermo Fisher Scientific) was used to determine the protein concentration. After denaturation at 95°C for 10 min, samples were loaded on 4–15% polyacrylamide gels (Bio-Rad), transferred to PVDF membranes (Millipore Sigma), and immunoblotted for protein expression using the following antibodies: guinea pig anti-GLT1 at 1:25,000 (catalog #AB1783, Millipore) and mouse anti-β actin at 1:20,000 (catalog #A1978, Sigma-Aldrich), and the following fluorescent secondaries: donkey anti-rabbit IRDye 800CW (LI-COR) at 1:10,000 and Goat anti-Mouse IRDye 680RD (LI-COR). Immunoreactive bands were imaged with LI-COR Odyssey and quantified using ImageJ software. Protein levels were normalized to actin levels. Normalized values were standardized by using the ratio of the left hemisphere, injected with viral solution, to the right noninjected hemisphere.

Quantitative qRT-PCR

Left M1 cortices were extracted as described above and homogenized in TRIzol (Invitrogen) using a high-speed homogenizer (FastPrep-24 5G Instrument, MP Biomedicals). Total RNA was isolated using phenol-chloroform extraction and then purified and concentrated using ethanol precipitation and washing on a silica column (RNA Clean & Concentrator-5, Zymo Research). Total RNA samples were reverse transcribed (SuperScirpt IV VILO, Thermo Fisher Scientific). The qRT-PCR was perfomed using a QuantStudio 3 System (Thermo Fisher Scientific) with PowerUp SYBR Green Master Mix (Thermo Fisher Scientific). The following primers were used: Glyceraldehyde 3-phosphate dehydrogenase (*Gapdh*) Forward, AAGAGAGGCCCTATCCCAAC, Reverse, GCAGCGAACTTTATT GATGG; peptidylprolyl isomerase A (*Ppia*) Forward, GTGACTTT ACACGCCATAATG, Reverse: ACAAGATGCCAGGACCTGTAT; solute carrier family 1, member 2 (*Slc1a2*) Forward: GAACGAGGCC CCTGAAGAAA, Reverse: CCTGTTCACCCATCTTCCCC; solute carrier family 1, member 3 (*Slc1a3*), Forward: GTAACCCGGAA GAACCCCTG, Reverse: GTGATGCGTTTGTCCACACC; solute carrier family 6, member 1 (*Slc6a1*), Forward, CACTCTGTTCTGG TGTCCCC, Reverse, GGGAAGCTTAATGCCAGGGT; solute carrier family 6, member 11 (*Slc6a11*), Forward, ATGATGCCCCTCTC TCCACT, Reverse, TACCACGGCTGTCACAAGAC; solute carrier family 6, member 6 (*Slc6a6*), Forward, TTCAGACAACAGACA CGCGA, Reverse, CTCGGCAGCAACCAGGTC; testican-2 (*Spock2*), Forward, AGGTCACATTTCAGCCACGA, Reverse, TTGATGTCC TTCCCTCCACC; basigin (*Bsg*) Forward, GGCGGGCACCATC

CAAA, Reverse, CCTTGCCACCTCTCATCCAG. Every sample was run in technical duplicate or triplicate. Relative expression was quantified using the $\Delta\Delta$Cp method.

RNAseq

Wild-type mice were water restricted and then trained for 0 (naive), 3 (novice) or 19 (expert) days. To control for stress levels, all three groups were water restricted and head fixed for the same duration as the expert mice. M1 cortices were then dissected as described above, but using ice-cold ACSF containing the following (in mM): 120 NaCl, 3 KCL, 26.2 NaHCO3, 2 MgSO$_4$, 0.2 CaCl2, 11.1 D-Glucose, 5 HEPES) bubbled with oxygen and supplemented with 0.02 AP5 and 0.02 CNQX instead of PBS. Cells were dissociated using Neural Tissue Dissociation Kit–Postnatal Neurons (catalog #130-094-802, Miltenyi Biotec) and gentleMACS Dissociator following manufacturer protocols. Cell suspension was depleted of microglia and myelin debris (Myelin Removal Kit, catalog #130096733, Miltenyi Biotec), then astrocytes were isolated using the anti-ACSA-2 magnetic cell sorting kit and protocol (catalog #130097678, Miltenyi Biotec). RNA was purified and concentrated with proteinase K cell digestion, ethanol precipitation, and washing on a silica column (Quick-RNA FFPE, Zymo Research). RNA concentration and quality were assessed with Agilent 2100 Bioanalyzer. Indexed cDNA libraries were generated using the SMARTer Stranded Total RNA-Seq Kit version 2 (catalog #634411, Illumina), and multiplexed sequencing was performed on Illumina HiSeq 2000. Reads were aligned to the mouse mm9 genome using the TopHat sliced read mapper (Trapnell et al., 2012). Fragment counts were obtained using the Cufflinks pipeline (Trapnell et al., 2012). Genes with fragment counts above 20 kpm were selected for further analysis. To remove unwanted variation, normalization was implemented using the Bioconductor packages EDASeq (Risso et al., 2011) and RUVSeq (Risso et al., 2014). Differential expression analysis was performed using Bioconductor package EdgeR, using a significance threshold of $p < 0.05$, which was then corrected for multiple comparisons (Robinson et al., 2010). The Gene Ontology (GO) analysis of DEGs was performed using PANTHER (Mi et al., 2019). The gene set enrichment analysis (GSEA) was performed using the Bioconductor EdgeR Camera package (Wu and Smyth, 2012). The data are available at the Gene Expression Omnibus repository (accession #GSE156661).

Experimental design and statistical analysis

All experiments included at least three replicates, with each replicate being a mouse-averaged value if not otherwise stated. Line plots and bar graphs show mean $\pm$ SEM. Box plot bars represent the median, the box extends from the 25th to 75th percentiles, and whiskers show 10th to the 90th percentile. No statistical methods were used to predetermine sample size. We used sample sizes similar to those in the literature in the field. Sample sizes provided at least 80% power to detect the experimental effect. For datasets with two data groups, groups were compared using Student's two-tailed t tests or Mann–Whitney U tests. Paired comparisons were performed with paired t test or paired Wilcoxon rank sum test. Comparisons of cumulative distributions were performed using a nonparametric Kolmogorov–Smirnov test. For datasets with three of more data groups, groups were compared using one-way ANOVA with multiple-comparisons test. Datasets with different treatment groups or different models built on grouped data were compared with (treatment/model) × astrocyte group two-way ANOVA, either with or without linear mixed model for individual animal effects, as indicated in the text. Results of statistical tests are reported in the figure legends, and values and replicate numbers are defined in the figure legends.

Results

Decreased GLT1 levels in M1 astrocytes alter movement trajectories

We trained mice to perform a cued lever push task (Peters et al., 2014) in which a lever press beyond a set threshold following trial start was rewarded with a water droplet (Fig. 1A). In mice trained daily in the lever push task, wild-type (WT) mice
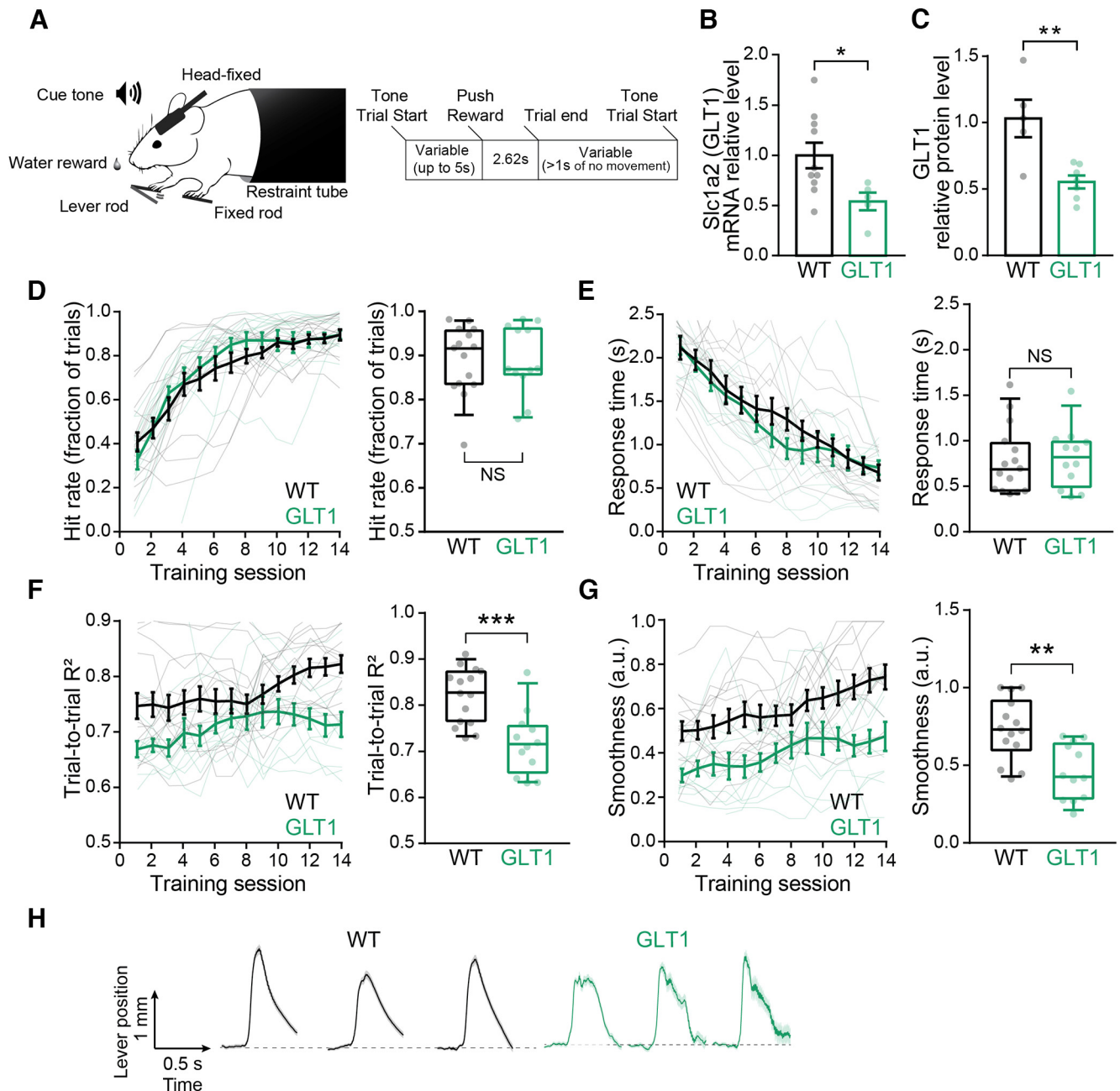
Figure 1. Decreased GLT1 levels in M1 astrocytes alter movement trajectories. **A,** The lever push task schematic. An auditory tone indicated trial start, and a lever push within 5 s was rewarded with a drop of water. A window of 2.62 s followed a push (correct trial) to allow for reward collection licking, or the trial would time out after 5 s (incorrect trial). Following either outcome, a 1 s intertrial interval of no movement triggered start of the next trial. **B, C,** GLT1 mice show a 46% reduction of Slc1a2 (Glt1) mRNA levels compared with WT (n = 10 WT mice, 6 GLT1 mice, ratio = 0.5401 ± 0.0882, *p = 0.0337, unpaired t test), as measured by qRT-PCR. Bar plots represent mean ± SEM; dots represent single observations. GLT1 mice (**C**) show a 45% reduction of GLT1 protein level (n = 6 WT, 8 GLT1 mice, ratio = 0.5535 ± 0.04859, **p = 0.0045, unpaired t test), as measured by Western Blot. **D,** GLT1 reduction in M1 astrocytes has no effect on hit rate. Left, All training sessions. Right, Average of expert sessions (training days 12–14; WT, mean = 0.8892 ± 0.01968; GLT1, mean = 0.8847 ± 0.01774; NS, not significant, p = 0.984, unpaired t test). For this figure, N = 15 WT, 12 GLT1 mice; box plot bar represents median, box extends from the 25th to 75th percentile, and whiskers show 10th to the 90th percentile. Data points for each individual mouse are shown. **E,** GLT1 reduction has no effect on response time. Left, All training sessions. Right, Average of expert sessions (WT, mean = 0.7739 ± 0.0682; GLT1, mean = 0.7905 ± 0.06986; NS, not significant, p = 0.8384, unpaired t test). **F–H,** Reduced GLT1 in M1 astrocytes perturbs learning of stereotyped and smooth movement trajectories. **F,** Trial-to-trial movement similarity estimated by the average pairwise correlation of the movement traces (trial-to-trial R^2). Left, All training sessions. Right, Expert sessions average (WT, mean WT = 0.8204 ± 0.01064; GLT1, mean = 0.7137 ± 0.0139; ***p = 0.0004, unpaired t test). **G,** Average movement smoothness estimated by the inverse of the number of push events per movement. Left, All training sessions. Right, Expert sessions average (WT, mean = 0.7325 ± 0.03158; GLT1, mean = 0.4585 ± 0.03156; **p = 0.0012, unpaired t test). **H,** Example average lever trajectory traces of three expert training sessions for one WT (black) and one GLT1 (green) example mouse.

improved their success rate with training time, starting with a phase of rapid learning by day 3 (novice mice) and reaching a performance plateau after 2 weeks of training (expert mice); correspondingly, response time decreased with training (Fig. 1D,E). Additionally, the lever push movements became smoother,

indicating an acquired dexterity that may contribute to a more stereotyped (more similar across trials) lever trajectory (Fig. 1F–H). These two outcomes represent two aspects of learning that are measured in this task—learning the cue association with movement and acquisition of the movement trajectory itself.

GLT1 critically influences synaptic transmission, as shown *in vitro* and in slices *in situ* (Rothstein et al., 1996; Tanaka et al., 1997; Arnth-Jensen et al., 2002; Huang et al., 2004; Tsukada et al., 2005; Takayasu et al., 2006; Tzingounis and Wadiche, 2007; Cui et al., 2014; Aida et al., 2015; Murphy-Royal et al., 2017). Moreover, GLT1 in astrocytes has an important role in neuronal plasticity, as demonstrated *in situ* (Oliet et al., 2001; Tsvetkov et al., 2004; Filosa et al., 2009; Omrani et al., 2009). Although mouse models of GLT1 knockdown have shown major behavioral deficits, previous studies largely involved brainwide and complete knockdown (Niederberger et al., 2003; Pardo et al., 2006; Cui et al., 2014; Aida et al., 2015; Gomez et al., 2019). To specifically explore the role of GLT1 expression in M1 astrocytes *in vivo* during motor learning, we delivered a viral vector encoding the CRE-recombinase under the astrocyte-specific GFAP promoter unilaterally in M1 cortex of GLT1-flox heterozygous mice (GLT1) and their wild-type littermates. Two weeks after injection, the expression level of GLT1 was decreased to ~50% at both mRNA and protein levels (mRNA ratio = 0.54 ± 0.088, WT, $n = 10$; GLT1, $n = 6$; protein ratio = 0.55 ± 0.049, WT, $n = 6$; GLT1, $n = 8$; Fig. 1B,C).

GLT1 mice had similar success rates and response times as WT controls (Fig. 1D,E), suggesting that association of the cue with movement is not affected. However, GLT1 mice showed deficits in learning-associated stereotyped movements, as indicated at training days 12–14 by the reduced average pairwise trial-to-trial similarity of the movement trajectory (average pairwise correlation WT, 0.82 ± 0.011, $n = 15$; GLT1, 0.71 ± 0.014, $n = 12$) and low dexterity (smoothness coefficient WT, 0.73 ± 0.031, $n = 15$; GLT1, 0.46 ± 0.032, $n = 12$; Fig. 1F–H). Thus, a reduction of astrocyte GLT1 expression in M1 is sufficient to perturb the stereotypy and smoothness of movement trajectories that accompany motor learning without affecting other aspects of learning in this task.

Astrocyte Gq pathway activation in M1 impairs task performance

Gq pathway activation in astrocytes has diverse effects on astrocytes, affecting calcium release from intracellular stores, astrocyte-neuron functions. and specific behaviors (Agulhon et al., 2013; Cao et al., 2013; Scofield et al., 2015; Chen et al., 2016; Martin-Fernandez et al., 2017; Adamsky et al., 2018; Yu et al., 2018; Iwai et al., 2021; Nagai et al., 2021). To explore the effect of the Gq pathway in M1 astrocytes, we used an engineered Gq-coupled designer receptor exclusively activated by designer drugs (DREADD), hM3Dq, which can be activated by exogenous CNO in a time-restricted manner (Armbruster et al., 2007; Roth, 2016). To induce pathway activation during behavior and *in vivo* imaging, we injected a viral hM3Dq-mCherry construct unilaterally in M1 in mice expressing the astrocyte-specific GFAP promoter. Costaining with astrocyte marker S100β showed high specificity and high density of expressing cells (>98%; Fig. 2A).

Activation of Gq-DREADD-expressing astrocytes on CNO application has been shown in brain slices to induce a release of calcium from the intracellular stores and an increase of intracellular calcium signaling (Agulhon et al., 2013). We injected unilaterally in M1 a viral GFAP-hM3Dq-mCherry construct in astrocyte-specific cytoplasmic GCaMP-expressing mice (GFAP-GCaMP5G mouse line) to image *in vivo* calcium activity in astrocytes 30 min after intraperitoneal injection of CNO. We observed that a low dose of CNO triggered an increase in intracellular calcium as measured by the baseline GCaMP fluorescence (Fig. 2B), along with a decrease in frequency and amplitude of calcium

events (Fig. 2C–E), consistent with near saturation of signaling because of the depletion of internal calcium stores. Similarly, a recent study found that Gq-DREADD activation in cortical astrocytes almost completely abolished calcium dynamics (Vaidyanathan et al., 2021).

We trained Gq-DREADD-expressing mice (Gq) and controls (CTRLs) in the lever push task. Two weeks after virus injection, mice were trained daily for 14 d of training sessions with an intraperitoneal injection of a low dose of CNO 30 min before training started. Training was continued for six additional days with an injection of vehicle (saline) solution instead of CNO. Gq mice injected with CNO showed a decreased performance rate (average hit rate, Gq + CNO, 0.64 ± 0.038, $n = 7$; CTRL + CNO, 0.81 ± 0.029, $n = 13$) as measured by the fraction of successful trials, which improved rapidly after withdrawal of CNO (saline injection; average hit rate, Gq + saline, 0.82 ± 0.032, $n = 7$; Fig. 2F). Gq mice injected with CNO also had increased response times (average response time, Gq + CNO, 1.46 ± 0.10, $n = 7$; CTRL + CNO, 0.71 ± 0.077, $n = 13$) that improved on CNO withdrawal (average response time, Gq + saline, 1.02 ± 0.13, $n = 7$; Fig. 2G). Because hit rate and response time were not fully rescued by CNO withdrawal, we examined a CNO-independent effect of Gq-DREADD by injecting a separate cohort of Gq mice with saline 30 min before each session throughout training. We did not observe any overt differences between Gq plus saline and control (data not shown), which may suggest that the residual effects on behavioral performance in Gq-DREADD mice treated with CNO are the result of lasting disruption of Gq signaling in astrocytes.

Finally, Gq mice showed a decreased stereotypy of movement, as indicated by the lower average pairwise trial-to-trial similarity of the movement trajectories (average pairwise correlation, CTRL + CNO, 0.73 ± 0.013 $n = 13$; Gq + CNO, 0.68 ± 0.016, $n = 7$). This was rescued by withdrawal of CNO (average pairwise correlation, Gq + saline, 0.75 ± 0.016, $n = 7$; Fig. 2G,I). However, we did not observe any significant difference in movement smoothness (Fig. 2H,I). Thus, Gq signaling activation in M1 astrocytes during motor learning is sufficient to temporarily perturb task performance by decreasing performance rate, slowing responses, and reducing the stereotypy of movement trajectories.

Decreased GLT1 levels in M1 astrocytes reduce neuronal signal correlations

GLT1 knockdown has been shown to drive neuronal hyperexcitability by dysregulating synaptic transmission in a number of brain regions (Rothstein et al., 1996; Tanaka et al., 1997; Oliet et al., 2001; Arnth-Jensen et al., 2002; Huang et al., 2004; Tsukada et al., 2005; Takayasu et al., 2006; Tzingounis and Wadiche, 2007; Filosa et al., 2009; Omrani et al., 2009; Aida et al., 2015). Given our finding that decreased GLT1 expression levels in M1 astrocytes affected the learning and execution of movement trajectories, we examined the effects of GLT1 astrocyte deficiency on M1 layer 2/3 neuron activity *in vivo*. Previous studies have shown that in WT mice, layer 2/3 neurons show plasticity associated with learning the lever push task, with the emergence of an ensemble of correlated neurons associated with the learned movement (Peters et al., 2014). We used two-photon imaging and the calcium indicator GCaMP6s to record the calcium activity of M1 layer 2/3 neurons during the lever push task in expert animals (Fig. 3A; Movie 1). We found that the average neuronal activity pattern during successful trials was similar in WT and GLT1 mice, with very low activity at
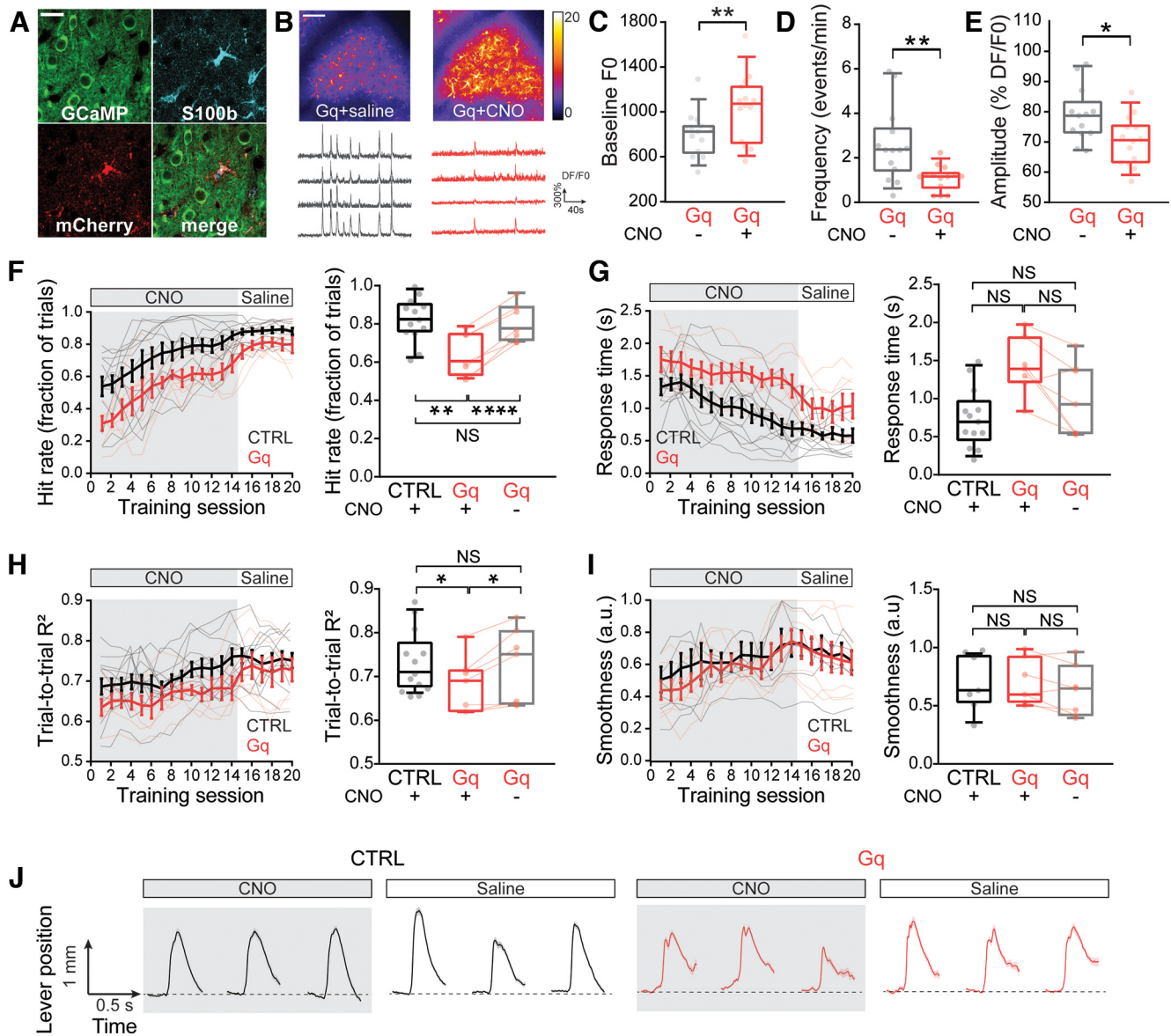
Figure 2. Astrocyte Gq pathway activation in M1 impairs task performance **A**, h3MD(Gq)-mCherry colocalized with immunohistochemistry labeling of astrocyte marker S100β but not with neuronal GCAMP. Scale bar, 25 μm. **B**, Gq activation increased the levels of cytoplasmic calcium. The same field of views containing AAV-GFAP-h3MD(Gq)-mCherry-expressing astrocytes (Gq) in naive (untrained) GFAP-GCaMP5G mice were imaged over 10 min passive sessions, 24 h apart, and 30 min after intraperitoneal injection of vehicle (saline) or CNO. Left, Color maps of the projection of the average GCAMP fluorescence (color bar) in astrocytes in a 10 min imaging session. Example astrocyte GCaMP fluorescence imaging sessions (24 h apart) of the same field of view, 30 min after intraperitoneal injection of either CNO or vehicle (saline). Scale bar, 100 μm. Bottom: Example astrocyte ROI raw DF/F0 traces (black, Gq + saline; red, Gq + CNO). **C**, Quantification of calcium baseline levels (average GCAMP fluorescence) from the three imaging sessions ($n = 14$ nonoverlapping fields of view from 5 mice, Gq + saline (- CNO), mean = 802.8 ± 53.07; Gq + CNO, mean = 1043 ± 80.06, **$p = 0.0093$, paired t test). **D**, Frequency of spontaneous calcium events ($n = 14$ nonoverlapping fields of view from 5 mice; Gq + saline, mean = 2.596 ± 0.4362; Gq + CNO, mean = 1.11 ± 0.1487, **$p = 0.0045$, paired t test). **E**, Quantification of the average event amplitude (DF/F0; $n = 14$ nonoverlapping fields of view from 5 mice; Gq + saline (- CNO), mean = 78.87 ± 2.490; Gq + CNO, mean = 70.26 ± 2.178, *$p = 0.0357$, paired t test). Box plots as defined in Fig. 1D; paired values from the same subject are connected with a line. **F–J**, Mice expressing GFAP-h3MD(Gq)-mCherry (Gq) and CTRLs were injected intraperitoneally 30 min before a training session started with a low dose of CNO for the first 14 training days, then with saline solution for 6 additional training days. For this figure, $N = 13$ CTRL, 7 Gq mice and data indicated as Gq - CNO are the Gq + saline group. **F**, Gq activation in M1 astrocytes reduces hit rate. Left, All training sessions. Right, Average of expert sessions (data from training days 12–14 and 18–20); CTRL + CNO, mean = 0.8127 ± 0.02985; Gq + CNO, mean = 0.6445 ± 0.03813; Gq + saline, mean = 0.8205 ± 0.03272; CTRL + CNO vs Gq + CNO, **$p = 0.0062$; CTRL + CNO vs Gq + saline, NS, not significant, $p = 0.9660$, Tukey's multiple comparisons, one-way ANOVA; Gq + CNO vs Gq + saline, ****$p < 0.0001$, paired t test). **G**, Gq activation increases response time. Left, All training sessions. Right, Average of expert sessions (CTRL + CNO, mean = 0.7104 ± 0.07735; Gq + CNO, mean = 1.458 ± 0.1039; Gq + saline, mean = 1.02 ± 0.1249; CTRL + CNO vs Gq + CNO, **$p = 0.0048$, CTRL + CNO vs Gq + saline, NS, not significant, $p = 0.3961$, Tukey's multiple comparisons, one-way ANOVA; Gq + CNO vs Gq + saline, *$p = 0.0225$, paired t test). **H–J**, Gq activation in M1 astrocytes perturbs movement trajectories. **H**, Trial-to-trial movement similarity. Right, Average of expert sessions (CTRL + CNO, mean = 0.73 ± 0.01295; Gq + CNO, mean = 0.681 ± 0.01631; Gq + saline, mean = 0.7467 ± 0.01579; CTRL + CNO vs Gq + CNO, *$p = 0.0493$; CTRL + CNO vs Gq + saline, NS, not significant, $p = 0.9668$, Tukey's multiple comparisons, one-way ANOVA; Gq + CNO vs Gq + saline *$p = 0.0111$, paired t test). **I**, Average movement smoothness. Left, All training sessions. Right, Average of expert sessions (CTRL + CNO, mean = 0.6999 ± 0.04929; Gq + CNO, mean = 0.7005 ± 0.04288; Gq + saline, mean = 0.6999 ± 0.04929; CTRL + CNO vs Gq + CNO, NS, not significant, $p > 0.999$; CTRL + CNO vs Gq + saline, NS, not significant, $p = 0.8073$, Tukey's multiple comparisons, one-way ANOVA; Gq + CNO vs Gq + saline, NS, not significant, $p = 0.0855$, paired t test). **J**, Example average movement trace of three expert training sessions with CNO or saline injection, for one CTRL (black) and one Gq (red) example mouse.
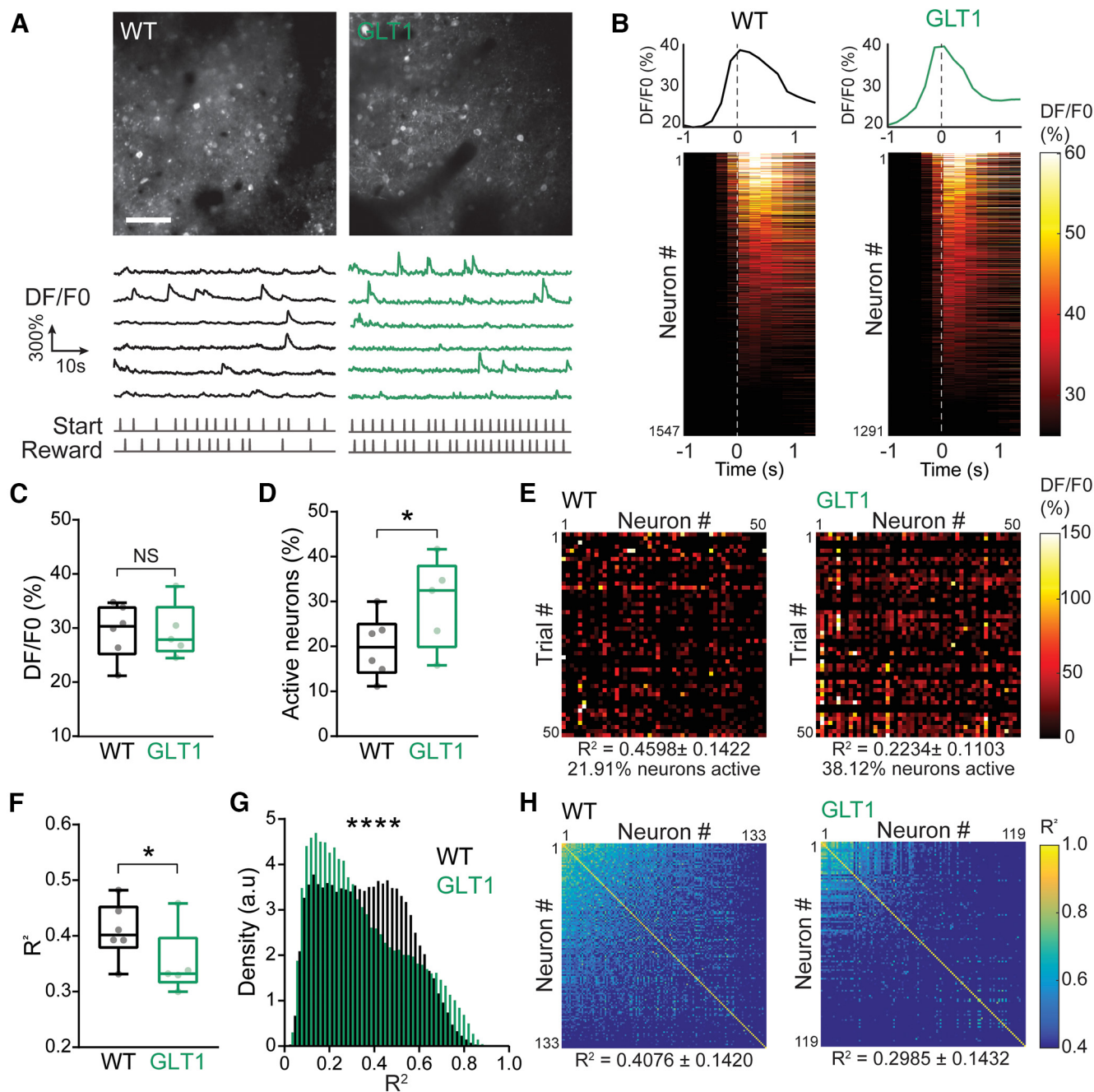
Figure 3. Decreased GLT1 levels in M1 astrocytes reduce neuronal signal correlations. *A–C*, Decreased GLT1 does not significantly change average neuronal activity. *A*, Top, Example field of view of neuronal GCaMP6s two-photon imaging *in vivo* (Movie 1). Scale bar, 25 µm. Bottom, Example raw DF/F0 traces. *B*, Aligned trial-averaged responses of M1 layer 2/3 neurons; WT, *n* = 1547 neurons from 15 nonoverlapping fields of view from 6 mice; GLT1, *n* = 1291 neurons from 13 nonoverlapping fields of view from 5 mice, from expert session training days 10–14. Top, Average DF/F0 trace over the movement epoch. Bottom, Normalized DF/F0 color map; neurons are sorted by maximum activity. Zero (0) on *x*-axis and vertical dashed line indicate time when lever position reached the reward threshold (1 mm). *C*, Average trial activity (DF/F0; WT, mean = 29.41 ± 2.053; GLT1, mean = 29.41 ± 2.281, NS, not significant, *p* = 0.9987, unpaired *t* test). *D*, Decreased astrocyte GLT1 increases the proportion of active neurons during the movement period. Neurons were defined as active during the movement period if the activity during movement (1 s period) was 2 SDs above the activity during ITI (1 s period). Percentage of movement-related neurons was calculated for each trial and then averaged across all trials. Percentage of active neurons during lever push is higher in GLT1 mice than WT (WT, mean = 19.89 ± 1.89; GLT1, mean = 29.62 ± 3.01, *p* = 0.0103, unpaired *t* test). *E*, Example color maps of trial-averaged activity for the first 50 trials for 50 neurons recorded in one expert training session. Neuron-to-neuron average pairwise correlation *R*² values and percentage of active neurons are indicated below each matrix. *F–H*, Decreased astrocyte GLT1 reduces neuronal signal correlations. *F*, Trial-to-trial activity similarity was measured by the average pairwise correlation of single-neuron activity vectors of concatenated trials. GLT1 mice have significantly lower average pairwise signal correlation (WT, mean = 0.4091 ± 0.01415; GLT1, mean = 0.3516 ± 0.01835, *p* = 0.0204, unpaired *t* test). *G*, Density histograms of pairwise neuronal correlation distribution (****p* < 0.001, Kolmogorov–Smirnov test). *H*, Example sorted correlation matrices of neuron-to-neuron average pairwise correlations for all neurons of one example session/field of view. Neuron-to-neuron average pairwise correlation *R*² values of the examples are indicated. For this figure, *N* = 6 WT, 5 GLT1 mice; box plots as described in Fig. 1*D*.

baseline (no movement) and an elevation of the calcium signal during the lever push movement period (Fig. 3*B*,*C*). However, GLT1 mice showed an increased percentage of neurons that were active during the movement epoch of each

trial compared with WT (WT, 19.89% ± 1.89, *n* = 6 mice; GLT1, 29.62% ± 3.01, *n* = 5 mice; Fig. 3*D*,*E*). Neuron-to-neuron signal correlation, measured by averaging the distance correlation coefficient between the concatenated trial
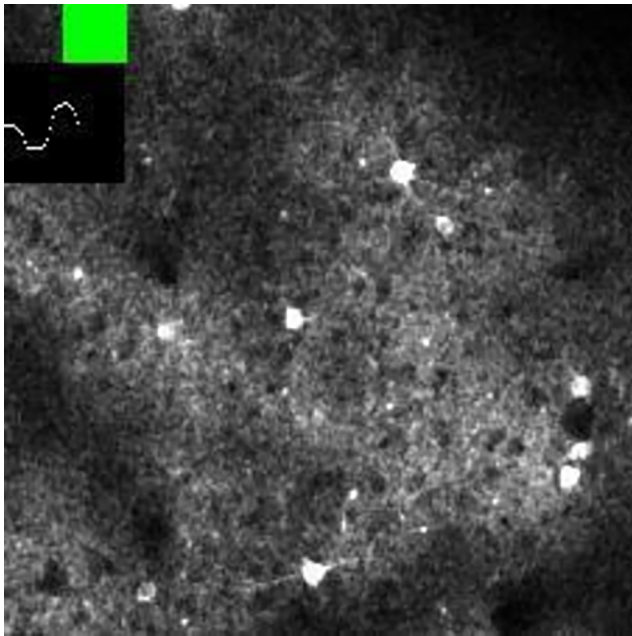
Movie 1. Example calcium imaging of M1 layer 2/3 neurons during expert training session. Overlay of lever position trace (white in black box), trial events (white square indicates trial start; green square indicates time when the lever passes the threshold and reward is delivered), and GCaMP6s fluorescence acquired by two-photon microscopy in an awake, behaving, expert mouse. 274 × 274 μm field of view. Video speed 1×, 5 fps. [View online]

activity vectors of pairs of single neurons, was high for a subset of WT neurons, thus showing ensemble activity (Fig. 3F, G). Despite an increased percentage of active neurons during movement, a population of highly correlated neurons was not found in the GLT1 trained mice (WT, 0.4091 ± 0.01415, $n = 6$ mice; GLT1, 0.3516 ± 0.01835, $n = 5$ mice; Fig. 3H). Thus, M1 neurons in trained GLT1 mice show decreased correlated ensemble activity compared with WT mice.

Gq pathway activation in M1 astrocytes increases neuronal signal correlations

We also studied the calcium activity of M1 layer 2/3 neurons during movement execution in control and Gq mice at expert time points in response to CNO intraperitoneal injections (Fig. 4A–C). The activity patterns of the neuronal populations were similar in the two groups, and the fraction of active neurons in Gq mice injected with CNO was not significantly different from control mice injected with CNO (Fig. 4D,E). Contrary to what we observed in the GLT1 mice, Gq mice showed increased neuron-to-neuron signal correlation, with a larger fraction of the neurons being highly correlated (CTRL + CNO, 0.323 ± 0.02267, $n = 9$; Gq + CNO, mean = 0.4074 ± 0.02154, $n = 6$; Fig. 4F–H). Thus, Gq pathway activation in M1 astrocytes is sufficient to trigger increased correlated activity of M1 neurons.

Astrocyte manipulations modulate M1 neuronal encoding of movement trajectory and task parameters

Our behavioral findings showed that both astrocyte manipulations led to deficits in movement trajectory and, in the case of Gq mice but not GLT1 mice, affected hit rate and response time (Figs. 1, 2). To determine the deficit associated with these astrocyte manipulations at the neuronal coding level, we fitted decoding models of M1 neuron population activity

to the push trajectory (Fig. 5; see above, Materials and Methods). The control groups of the GLT1 inhibition and Gq activation cohorts had similar task performances, and therefore were pooled as the WT group for the decoding and encoding analyses. An SVR model was used to predict the push trajectory during each training session from neuronal population spiking rate (Fig. 5A,B). For each neuronal population sample, the predictive power of the decoding model was evaluated by calculating the mutual information (MI) between predicted trajectory and the actual push trajectory (Fig. 5C). In WT mice, the models produced more accurate predictions of lever movement trajectories, whereas in both Gq and GLT1 neuronal populations, the MI values between predicted and actual trajectories were significantly lower than that of WT neuron populations (median values binned by animals, WT, 0.219; GLT1, 0.054; Gq, 0.052). These results indicate that in M1, astrocyte-specific manipulations of glutamate transport and Gq signaling reduce neuronal population encoding of movement trajectory.

Because M1 neurons have been suggested to encode more than just directed movement signals (Doron and Brecht, 2015), we evaluated the encoding of specific behavioral features by single M1 neurons in WT, GLT1, and Gq mice. We created GLMs to predict individual neuronal activity during each trial from these specific behavioral features (Engelhard et al., 2019) and compared the prediction performance of the models among the three groups (Fig. 6; see above, Materials and Methods). The models used seven behavioral features as predictors, including two event variables, start and reward (or movement threshold); two whole-trial variables, hit/miss and response time; and three continuous variables, movement trajectory, movement speed, and a step function (moving) indicating whether the animal started moving in a trial (Fig. 6A). In WT mice, push speed, trial success (hit/miss), and response time were all predictive of the neuronal activity (median $R^2 > 1\%$), whereas the two event variables, the motion indicator and the raw movement trajectory, were not very predictive (median $R^2 < 1\%$; Fig. 6B,C). The full model with all seven behavioral features predicted less single-neuron activity variation and less encoding power for both GLT1 and Gq mice compared with WT (Fig. 6D; medians, WT, 0.104; GLT1, 0.066; Gq, 0.072). Moreover, the relative contribution of different behavioral features was altered in GLMs of neurons from GLT1 mice compared with WT mice, with a relative increase in the encoding of the response time in GLT1 neurons (Fig. 6E). This is consistent with the impaired movement trajectory but preserved response time and success rate observed for GLT1 mice (Fig. 1). In contrast, neurons from Gq mice showed an overall reduced but largely conserved relative contribution of different behavioral features (Fig. 6E), suggesting a generalized reduction of the encoding of task parameters. This is consistent with Gq mice showing behavioral impairments in both task performance and movement trajectory (Fig. 2).

Motor learning leads to modification of gene expression profiles in M1 astrocytes

Given our findings that astrocytes critically contribute to motor learning via GLT1 and calcium regulation, we assessed the molecular changes in astrocytes that correlated with motor learning. We used RNAseq to identify gene expression changes in M1 astrocytes as mice learn the lever push task. M1 cortices of mice were extracted after no training (untrained naive mice), training in the lever push task for 3 days (partially trained novice mice),
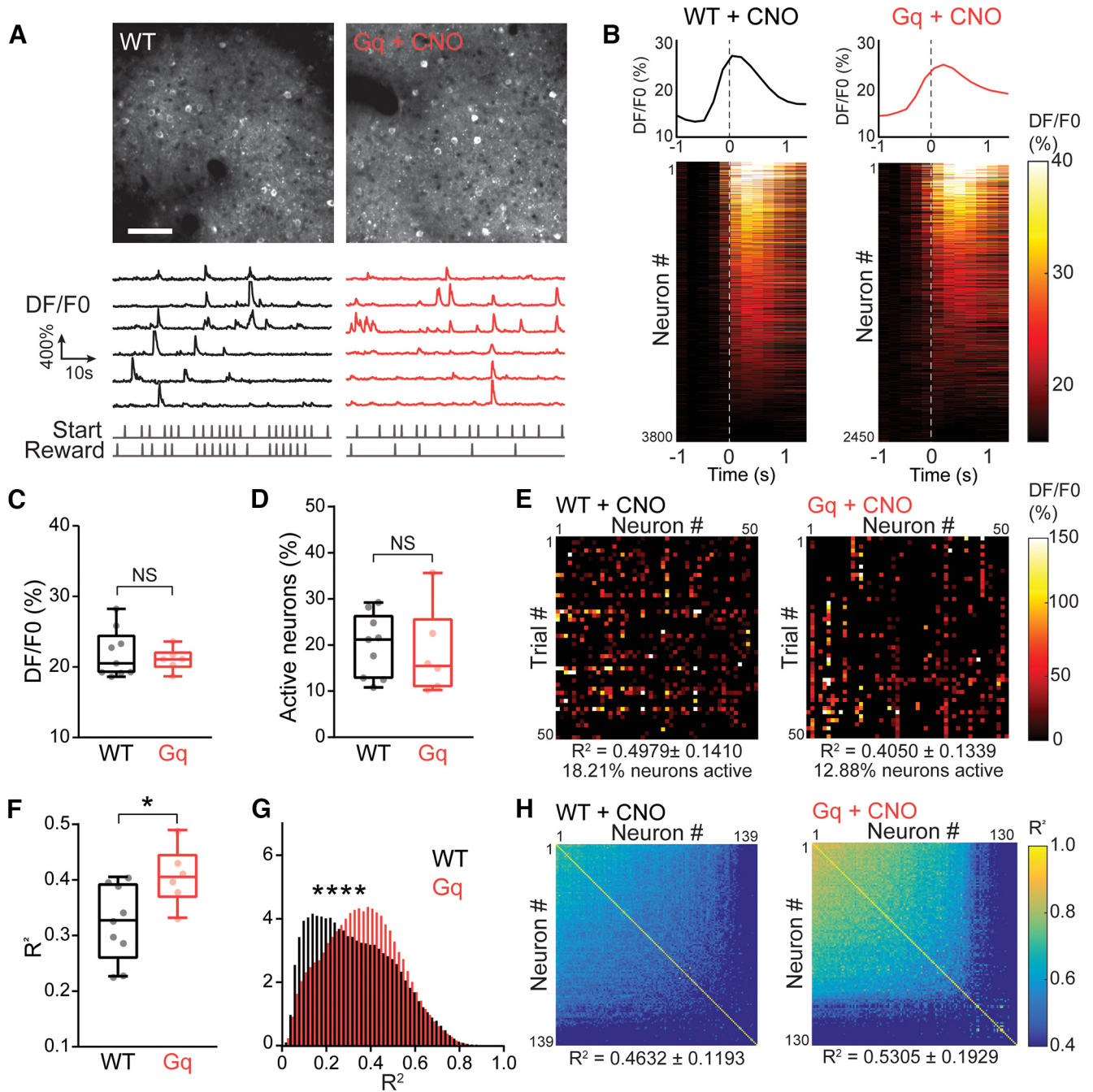
Figure 4. Gq pathway activation in M1 astrocytes increases neuronal signal correlations. ***A–C***, Astrocyte Gq activation does not significantly change average neuronal activity. ***A***, Top, Example field of view of neuronal GCaMP6s two-photon imaging *in vivo*. Scale bar, 25 μm. Bottom, Example raw DF/F0 traces. ***B***, Aligned trial-averaged responses of M1 layer 2/3 neurons. N = 3800 neurons from 9 CTRL mice injected with CNO, n = 2450 neurons from 6 Gq mice injected with CNO; data from expert sessions. Top, Average DF/F0 trace over movement epoch. Zero (0) on *x*-axis and vertical dashed line indicate time when lever position reached the reward threshold (1 mm). Bottom, Normalized DF/F0 color map; neurons are sorted by maximum activity. ***C***, Average trial activity (DF/F0; CTRL + CNO, mean = 21.87 ± 1.136; Gq + CNO, mean = 21.08 ± 0.6631, NS, $p = 0.6077$, unpaired *t* test). ***D***, Neurons were defined as active during the movement period if the activity during movement (1 s period) was 2 SDs above the activity during ITI (1 s period), and the percentage of movement-related neurons was calculated for each trial and then averaged across all trials. The percentage of active neurons during lever push movement was not significantly different between CTRL and Gq mice (CTRL + CNO, mean = 19.88 ± 2.286; Gq + CNO, mean = 18.41 ± 3.883, NS, $p = 0.7336$, unpaired *t* test). ***E***, Example color maps of trial average activity for the first 50 trials for 50 neurons recorded in one expert training session. Neuron-to-neuron average pairwise correlation R^2 values and percentage of active neurons of the examples are indicated below each matrix. ***F–H***, Astrocyte Gq activation increases neuronal signal correlations. ***F***, Trial-to-trial activity similarity was measured by the average pairwise correlation of single-neuron activity vectors of concatenated trials. (CTRL + CNO, mean = 0.323 ± 0.02267; Gq + CNO, mean = 0.4074 ± 0.02154, *$p = 0.0237$, unpaired *t* test). ***G***, Density histograms of pairwise neuronal correlation distribution (****$p < 0.0001$; Kolmogorov–Smirnov test). ***H***, Example sorted correlation matrices of neuron-to-neuron average pairwise correlations for all neurons of one example session/field of view. Neuron-to-neuron average pairwise correlation R^2 values of the examples are indicated. For this figure, n = 9 CTRL + CNO, 6 Gq + CNO mice, injected intraperitoneally 30 min before all training sessions with a low dose of CNO. Box plots as described in Figure 1D.
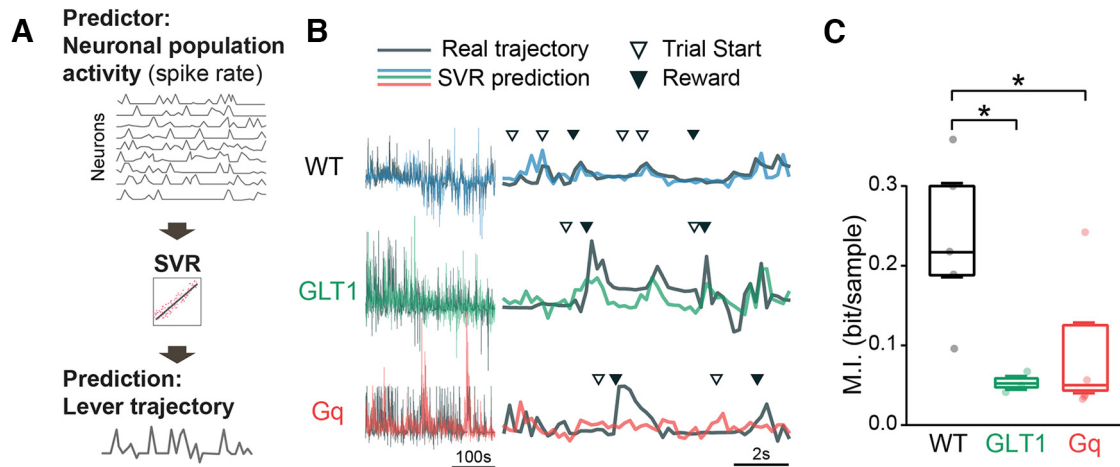
Figure 5. M1 neuronal population decoding of movement trajectories is affected by astrocyte manipulations. **A**, An SVR decoding model was used to predict the push trajectory during each training session from neuronal population spiking rate. **B**, Example lever movement traces decoded from the neuronal population activity, compared with actual traces. Black, actual movement trajectory; blue, decoded trace from WT animals; green, decoded trace from GLT1 animals; red, decoded trace from Gq animals. Left, Predicted and actual traces. Calibration, 100 s. Right, zoomed-in traces. Calibration, 2 s. Arrows indicate trial start (white) and reward or time when lever position reached reward threshold (black). **C**, Decoding performance (mutual information) was decreased in both GLT1 and Gq mice (N = 5/3/5 mice for WT/GLT1/Gq, respectively; WT, median = 0.219; GLT1, median = 0.054, *p = 0.0357, Mann–Whitney U test; WT, median = 0.219; Gq, median = 0.052, *p = 0.0318, Mann–Whitney U test). N = 13/11/16 nonoverlapping fields of view, 33–91 neurons per field of view, total 580/586/565 neurons and 734/911/631 trials from 5/3/5 WT/GLT1/Gq mice, respectively. Dots in the plot represent the average M.I. calculated per neuronal population and binned by animal. Box plots as defined in Figure 1D.

or training in the lever push task for 19 days (fully trained expert mice; Fig. 7A). To control for the absence of lever push movement and task training, all three groups were water restricted and head fixed for the same duration as the expert mice. Astrocytes were isolated using ACSA-2 immunomagnetic sorting (Holt and Olsen, 2016). We validated the isolation protocol by comparing the normalized gene counts of cell-type-specific markers for the three groups. Samples of all the groups were similarly enriched in astrocyte-specific genes and depleted of other brain cell markers (Fig. 7B). RNAseq was performed and results analyzed using the EdgeR package (Bioconductor) to identify (1) DEGs and (2) significantly enriched gene sets in astrocytes from novice and expert mice compared with naive mice (Fig. 7C). We found 27 DEGs in novice mice and 36 DEGs in expert mice (p value < 0.05) with an overlap of 11 DEGs (Fig. 7D; Extended Data Table 7-1). The numbers of DEGs that were upregulated or downregulated were similar between novice and expert groups (Fig. 7D). We then used the PANTHER classification system to analyze the DEG list (Mi et al., 2019). Several GO biological processes and molecular functions were enriched in the DEG list of known protein coding genes (Extended Data Table 7-2). The differentially regulated GO categories were mostly related to metabolism, transcription, and signaling. Moreover, DEGs were significantly enriched in membrane or extracellular protein coding genes, suggesting the importance of transporters, receptors, and cell–cell communication (Extended Data Table 7-2), similar to previously described datasets from other brain regions (Chai et al., 2017; Hasel et al., 2017; Farhy-Tselnicker et al., 2021).

We performed a GSEA of the RNAseq data, which identifies sets of genes with small individual expression changes that may not be detected using DEG analysis but collectively contribute to the dysregulation of a shared biological function (GO category). We identified 99 and 100 gene sets in novice and expert mice, respectively, that were significantly enriched relative to other genes in terms of differential expression (Fig. 7C; Extended Data Table 7-3). Most of the enriched gene sets were overlapping GO categories of transmembrane transporters such as Symporter Activity,

Secondary Active Transmembrane Transporter Activity, Amino Acid Transporter Activity, L-Glutamate Transmembrane Transport, Organic Acid Transmembrane Transport, and Sodium Ion Transmembrane Transporter (Fig. 7F). The GO: L-Glutamate Transport gene set contained only two genes, coding for the two astrocyte-specific glutamate transporters GLT1 (*Slc1a2*) and GLAST (*Slc1a3*), with high and low levels of cortical expression, respectively. Not only was this gene set significantly enriched, it was also included in most of the other enriched GO category sets (Fig. 7E). The GO: Solute Sodium Symporter Activity gene set was also contained in most of the enriched gene sets, with six genes expressed in M1 cortex samples including astrocyte-specific glutamate transporters (*Slc1a2*/GLT1 and *Slc1a3*/GLAST) and GABA transporters (*Slc6a1*/GAT1 and *Slc6a11*/GAT3; Extended Data Table 7-3). To control for the specificity of the observed changes to the forelimb M1 cortex, we performed the same experiment with left hindlimb M1 (hM1) cortex samples (data not shown). We observed no significant differences in hM1 expression levels for most genes, but we noted a trend for a few genes, and a significant change for one gene, *Slc6a1*, which is upregulated in both the forelimb and hindlimb motor cortex of expert mice, supporting the idea that large regions of mouse M1 and even wider swaths of cortex are partially activated during reward-related movement (Musall et al., 2019).

These results indicate that M1 cortical astrocytes undergo changes in gene expression associated with motor learning that may underlie mechanisms of astrocyte contributions to M1 function. Furthermore, they corroborate and highlight the importance of glutamate transporter modulation for our motor learning task.

Decreased GLT1 levels and astrocyte Gq pathway activation in M1 impair motor-learning-associated changes in gene expression

Based on the motor-learning-associated changes in transcriptomic expression of genes and gene sets in M1 astrocytes of wild-type mice (Fig. 7), we explored the expression of a selection of
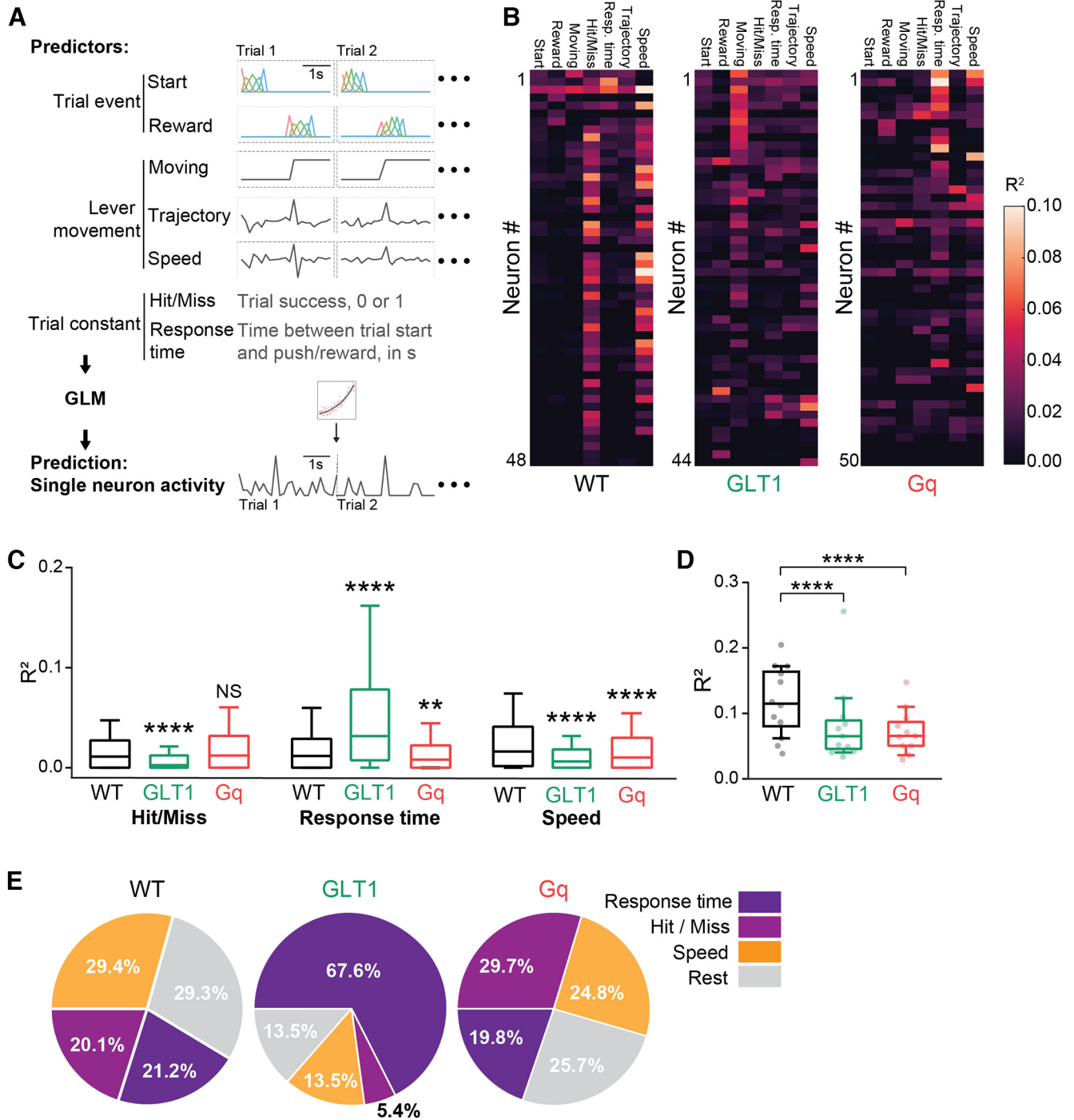
Figure 6. Astrocyte manipulations modulate M1 neuronal encoding of task parameters *A*, The GLM used to model neuronal encoding of task parameters. Predictors and predicted neuronal activity in an example trial. Seven predictors spanning trial event, lever movement, and trial constant were used (see above, Materials and Methods). Trials were concatenated, and one GLM was fit for each neuron, and the R^2 between predicted and actual neuronal activity was calculated for either a full model using all the above behavioral measures as predictors or a model with all but one behavioral feature. The difference between predictions from these two models was used to measure the contribution from the particular behavioral feature. $N = 580/586/565$ neurons, from 13/11/16 nonoverlapping fields of view, from 5/3/5 WT/GLT1/Gq mice, respectively. *B*, Representative single neurons encoding R^2 values from the seven predictors for WT, GLT1, and Gq mice. Rows represent individual neurons; columns represent the contribution of individual features. *C*, Encoding performance of the GLM for the behavioral features with $R^2 > 1\%$, Hit/Miss, response time, and speed. GLT1 mice showed less encoding of the trial outcome Hit/Miss (****$p = 1.17E\text{-}17$, Mann–Whitney U test), whereas Gq mice showed no significant difference from WT (NS, not significant, $p = 0.208$, Mann–Whitney U test). Response time was encoded less in Gq mice (****$p = 0.00201$, Mann–Whitney U test) but more in GLT1 mice (****$p = 1.38E\text{-}22$, Mann–Whitney U test), consistent with the behavioral differences observed in these mice. Both astrocyte manipulations reduced push speed encoding in M1 neurons (WT vs Gq, ****$p = 7.01E\text{-}6$; WT vs GLT1, ****$p = 2.62E\text{-}17$; Mann–Whitney U tests), consistent with the disruptive effect of Gq and GLT1 manipulations on push trajectory decoding. *D*, Single-neuron predictive power R^2 values from all features. Both astrocyte manipulations reduce the predictive power of the full model ($N = 13/11/16$ for WT/GLT1/Gq, respectively; WT, median $= 0.104$; GLT1, median $= 0.066$, $p = 2.15E\text{-}18$, Mann–Whitney U test; WT, median $= 0.104$; Gq, median $= 0.072$, $p = 3.14E\text{-}11$, Mann–Whitney U test). Box plots as defined in Figure 1. *E*, Pie chart comparison of mean R^2 across all neurons for the most predictive task features. The size of each section represents the mean neuronal encoding power for WT, GLT1, and Gq mice (from *C*). GLT1 mice show a change in the contribution profile of the predictors compared with WT mice, with a larger relative encoding contribution of response time and relative decrease in encoding of all other features. Gq mice showed a small relative increase in neuronal encoding of trial outcome (Hit/Miss) compared with WT mice, and in general, a reduced but globally conserved predictor contribution profile, suggesting a global reduction of encoding of all task parameters.
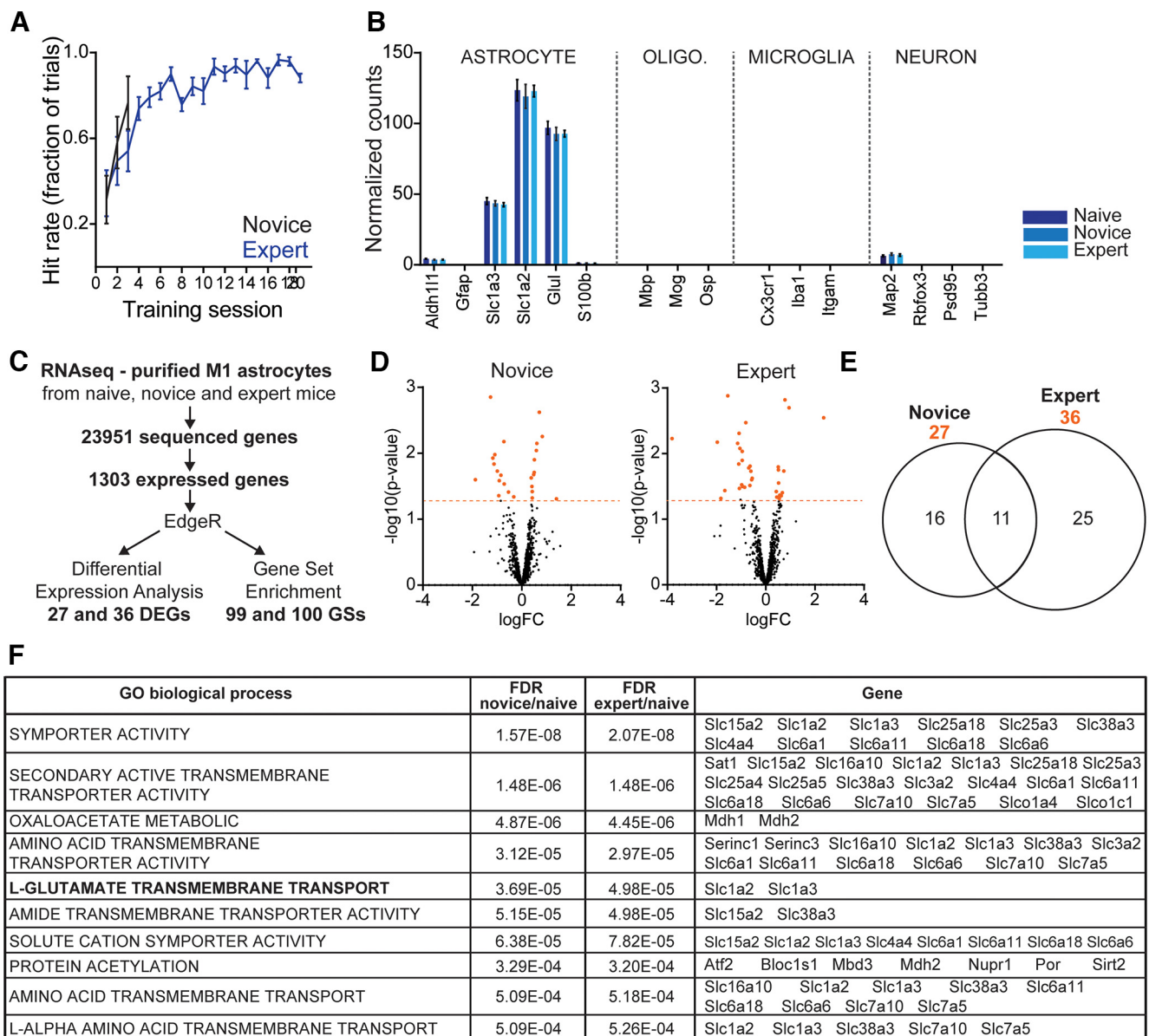
Figure 7. Motor learning leads to modification of gene expression profiles in M1 astrocytes. **A**, Learning curves of novice and expert mice trained in the lever push task and used for RNAseq experiments. Groups were named as follows: naive mice, not trained in the lever push task; novice mice, trained for 3 training sessions; and expert mice, trained for 19 training sessions and showing successful learning of the task. Graph represents hit rate (mean ± SEM) as measured by the fraction of correct trials; $n = 6$ wild-type mice for each group. **B**, Astrocyte purification was confirmed for the three groups by measures of the normalized gene expression of astrocyte, oligodendrocyte (OLIGO.), microglia, and neuron-specific genes. Gene expression was normalized by housekeeping gene counts (*Gapdh*). Bar plots represent mean ± SEM. **C**, Gene expression profiles from astrocytes of the three groups were analyzed and compared using the Bioconductor EdgeR package to perform DEGs and gene set enrichment analyses. Twenty-seven DEGs were identified in novice mice, 36 DEGs in expert mice (Extended Data Table 7-1). Ninety-nine gene sets in novice mice and 100 in expert mice were significantly enriched relative to naive mice, with an overlap of 98 GO categories (Extended Data Table 7-2). $N = 6$ wild-type mice for each of the three groups. **D**, We identified 27 DEGs in naive mice and 36 DEGs in expert mice; 11 DEGs were common for both. Volcano plots show logarithms of fold change (log2FC) and p value [-log10 (p value)] of differential expression of all expressed genes. Each dot represents one gene. Orange dots indicate DEGs (p value > 0.05) **E**, Venn diagram of DEGs. **F**, Top 10 significantly enriched gene sets differentially regulated in M1 astrocytes in novice and expert mice compared with naive mice and their respective expressed genes. In particular, the gene set corresponding to L-Glutamate Transmembrane Transport function (boldface) was significantly enriched (Extended Data Table 7-3).

these genes in Gq and GLT1 naive and expert mice (Fig. 8). Genes were selected from sets of previously identified DEGs (*Bsg*, *Spock2* and *Slc6a6*) and GSEA gene sets (*Slc1a2*, *Slc1a3* from GO: L-Glutamate Transmembrane Transport, and *Slc1a2*, *Slc1a3*, *Slc6a6*, *Slc6a1*, *Slc6a11* from GO: Solute Sodium Symporter Activity; Fig. 8A). First, all selected genes showed significant upregulation in expert WT mice compared with untrained (naive) WT mice, confirming the RNAseq results (Fig. 7D–F) in independent samples and experiments. In contrast, both GLT1 and Gq mice showed no learning-associated differences for the selected genes, with the exception of *Bsg*, which was significantly downregulated in GLT1 expert mice compared with GLT1 naive mice and significantly upregulated in Gq expert mice compared with Gq naive mice (Fig. 8A,C). *Slc1a2* (GLT1) was significantly downregulated in GLT1 mice as expected, but significantly upregulated in Gq mice (Fig. 8B). Thus, Gq activation and GLT1 reduction both impair motor-learning-associated gene expression changes, and the expression of some genes is oppositely regulated following these manipulations.
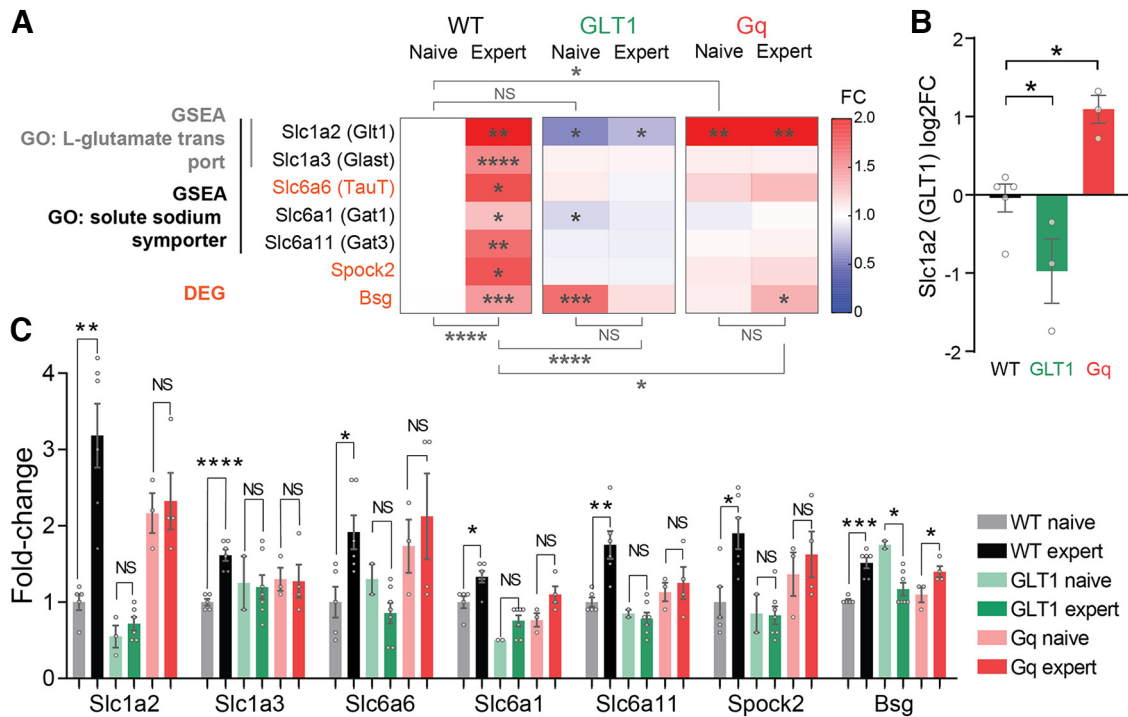
Figure 8. Decreased GLT1 levels and astrocyte Gq pathway activation in M1 impair motor-learning-associated changes in gene expression. *A*, Heat map of average gene expression fold change (FC) of selected genes, measured by qRT-PCR and normalized to wild-type naive mice. Genes were selected within RNAseq-identified DEGs (*Bsg, Spock2* and *Slc6a6*, highlighted in orange) and GSEA gene sets (*Slc1a2, Slc1a3* from GO: L glutamate transport, and *Slc1a2, Slc1a3, Slc6a6, Slc6a1*, and *Slc6a11* from GO: solute sodium symporter activity). In contrast to WT mice, GLT1 and Gq mice do not show motor-learning-associated changes in gene expression. Naive versus Expert, two-way ANOVA; WT, ****$p < 0.0001$; GLT1, NS, $p = 0.2338$; Gq, NS, not significant, $p = 0.1603$ for the variability explained by learning. Stars on the heat map indicate statistically significant differences for each individual gene in comparison with WT naive (one-way ANOVA with Dunnett's multiple comparisons test), stars below and above the heat map indicate statistical significance of the variability explained by the manipulation considering all genes (two-way ANOVA), and stars over the bar plot indicate statistical significance for the mean comparison of naive and expert expression levels for each individual gene. NS, not significant, $p > 0.05$, *$p < 0.05$, **$p < 0.01$, ***$p < 0.001$, ****$p < 0.0001$. *B*, *Slc1a2* is significantly downregulated in GLT1 naive mice and upregulated in Gq naive mice compared with WT naive mice. Logarithm of fold change (log2FC) is shown. Naive WT mice, mean = 0 ± 0.1792, $n = 5$; naive GLT1 mice, mean = −0.9738 ± 0.4123, $n = 3$; Gq naive, mean = 1.09 ± 0.1783, $n = 3$. WT versus GLT1, *$p = 0.0197$; WT versus Gq, *$p = 0.071$, Dunnett's multiple comparisons test, one-way ANOVA. *C*, Bar plot (mean ± SEM) representing the expression FC of selected genes in the forelimb motor cortex of WT, GLT1, and Gq mice, naive, and expert mice. qRT-PCR confirmed significantly increased expression levels of all selected genes in expert WT mice compared with naive WT mice ($n = 5$ naive WT mice, $n = 6$ expert WT mice). Compared with WT naive mice, *Slc1a2* is significantly downregulated in GLT1 naive and expert mice (WT naive, mean = 1 ± 0.1049, $n = 5$; GLT1 naive, mean = 0.55 ± 0.1443, $n = 3$, *$p = 0.0424$, unpaired *t* test; GLT1 expert, mean = 0.7167 ± 0.08724, $n = 5$, *$p = 0.0476$, Mann Whitney *U* test), and upregulated in Gq naive and expert mice (Gq naive, mean = 2.167 ± 0.2603, $n = 3$, **$p = 0.0026$, unpaired *t* test; Gq expert, mean = 2.325 ± 0.3705, $n = 4$, **$p = 0.0465$, unpaired *t* test). *Bsg* is the only gene that showed changes between naive and expert mice in GLT1 and Gq mice, with a downregulation associated with the learning in GLT1 mouse and an upregulation in Gq mice (GLT1, naive, mean = 1.75 ± 0.05, $n = 3$; expert, mean = 1.171 ± 0.08371, $n = 7$, *$p = 0.0101$, unpaired *t* test; Gq, naive, mean = 1.1 ± 0.1, $n = 3$; expert, mean = 1.40 ± 0.07071, $n = 4$, *$p = 0.0286$, Mann Whitney *U* test). Of note, *Bsg* is significantly upregulated in naive GLT1 mice and in expert Gq mice compared with WT naive mice (GLT1 naive, mean = 1.75 ± 0.05, $n = 3$, ****$p < 0.0001$, unpaired *t* test; Gq expert, mean = 1.40 ± 0.07071, $n = 4$, ***$p = 0.0007$, unpaired *t* test).

Discussion

The primary motor cortex is both a representation of and crucial for motor learning, accurate motor control, and motor dexterity (Nudo et al., 1996; Tennant et al., 2011; Kawai et al., 2015; Peters et al., 2017). Acquisition of a skilled motor movement is accompanied by increased structural (Chen et al., 2015; Cichon and Gan, 2015) and synaptic (Gloor et al., 2015; Hoshiba et al., 2017) plasticity, leading to the functional reorganization of neuronal networks (Georgopoulos et al., 1986; Dombeck et al., 2009; Harrison et al., 2012; Hira et al., 2013; Peters et al., 2014; Elsayed et al., 2016). Given the multitude of evidence that astrocyte function is associated with neuronal activity and synaptic plasticity during learning and behavior (Poskanzer and Yuste, 2016; Adamsky et al., 2018; Yu et al., 2018; Nagai et al., 2019; Corkrum et al., 2020; Hennes et al., 2020; Kol et al., 2020; Lines et al., 2020; Ackerman et al., 2021; Ribot et al., 2021; Zhou et al., 2021; Hösli et al., 2022), we asked whether astrocytes directly contributed to the plasticity and reorganization of motor cortex microcircuits that are associated with the acquisition of a skilled motor movement. Here, we interrogated astrocyte function, specifically

glutamate clearance or Gq signaling, in the context of performance and neuronal ensemble formation during the acquisition of a lever push movement. Mice expressing decreased levels of the astrocytic glutamate transporter GLT1 in M1 showed a normal success rate and response timing but a statistically significant decrease in the learning and execution of a stereotyped (reliable) and precise (smooth) movement trajectory. M1 neuronal population activity was strongly decorrelated and showed impaired encoding of movement trajectory. Encoding of task parameters by M1 neurons revealed a proportionately greater representation of response time, consistent with behavioral preservation of response time and success rates. Mice with Gq signaling activation in M1 astrocytes showed decreased success rate, delayed response time, and impaired learning and execution of the stereotyped movement in the same task. Their altered task performance was accompanied by high levels of nonencoding M1 neuronal signal correlation, reduced population encoding of movement trajectory, and nonspecific reduction of encoding of task parameters by single neurons. Using M1 as a test bed, these findings provide quantitative evidence

for the role of astrocytes in influencing information coding by single neurons and neuronal populations during learning.

The astrocytic glutamate transporter GLT1 is the major glutamate transporter in the cerebral cortex. Its role in regulating glutamate availability and accumulation of extracellular glutamate has been well documented, along with its role in limiting glutamate spillover to neighboring synapses and extrasynaptic receptors (Rothstein et al., 1996; Asztely et al., 1997; Diamond and Jahr, 1997; Tanaka et al., 1997; Bergles et al., 1999; Arnth-Jensen et al., 2002). Precise control of glutamatergic signaling is critical for synaptic plasticity (Katagiri et al., 2001; Barnes et al., 2020), and thus GLT1 function is one mechanism by which astrocytes influence neuronal activity and circuits during learning and behavior (Omrani et al., 2009; Bechtholt-Gompf et al., 2010; Aida et al., 2015; Valtcheva and Venance, 2019). Consistent with this role for astrocytes in modulating glutamate signaling to drive functional plasticity, we observed that decreasing GLT1 levels in M1 layer 2/3 astrocytes triggered an increase in the proportion of active neurons during the movement epoch of the task. However, these extra neurons contribute to noise rather than relevant neuronal ensemble information, as shown by the decrease in correlated neuronal population activity. Highly correlated populations of neurons are associated with development of a stereotyped and smooth lever push movement (Peters et al., 2014), and, accordingly, we observed here that GLT1 mice showed deficits in the lever push movement but preserved hit/miss performance in the task. This phenotype is similar to deficits observed after lesioning M1 before motor learning (Peters et al., 2014; Kawai et al., 2015), indicating that M1 circuitry is critical for the acquisition of skilled movements. Thus, our results, which show that GLT1 reduction alters activity in these circuits to reduce population encoding of movement trajectory and alter single neuron encoding of task parameters, further our understanding of M1 circuitry by pointing to a functional influence by astrocytes.

In contrast, astrocyte-specific Gq signaling activation in M1 astrocytes triggered an increase in neuronal signal correlation that also appeared to be noninformative. This suggests a crucial role for astrocytes in decorrelating neurons through Gq-dependent mechanisms. The behavioral phenotype was accompanied by a significant increase in response delay, decrease in the fraction of successful trials (hit rate), and decrease in stereotypy of the push trajectory. The failure of Gq-activated astrocytes to decorrelate neuronal activity in M1 layer 2/3 during motor learning may affect downstream neurons in charge of task execution, leading to delayed responses and reduced task performance. The behavioral phenotype was rapidly improved when astrocyte-specific Gq activation was stopped, suggesting that the perturbation was transient and reversible, and affected mechanisms of execution during motor learning rather than learning per se Together with our observations after GLT1 knockdown, the data suggest that an optimal level of neuronal correlation is required for the emergence of functional neuronal ensembles that drive task performance. In the two manipulations we performed, one increases neuronal correlations, whereas another decreases them. In both cases, movement trajectory is altered, suggesting that meaningful correlations that carry information are what drive motor learning, rather than the absolute magnitude of potentially nonspecific correlations.

The response time was the task parameter that showed the largest change with Gq activation in M1 astrocytes, and this was greatly improved but not completely restored in the CNO withdrawal group. One hypothesis is that the Gq-DREADD construct by itself (without CNO) had an effect. We thus tested a small

cohort of Gq-DREADD mice injected with saline throughout the learning of the task but did not see any difference from the control group. Another factor could be a lasting effect of the CNO despite withdrawal, either by direct residual presence in the cortex or by indirect effect on task performance through lasting functional or structural cellular changes.

Gq-GPCR is known to trigger intracellular calcium elevation through IP3-induced calcium release from the ER (Clapham, 2007; Mizuno and Itoh, 2009; Agulhon et al., 2013; Yu et al., 2018). We found that M1 astrocyte Gq activation was associated *in vivo* with an increase in intracellular calcium, likely triggering a saturation of calcium signals and consequently a decrease in frequency of calcium events. This result is consistent with a recent study demonstrating a similar decrease in calcium dynamics in Gq-activated cortical astrocytes (Vaidyanathan et al., 2021). We note that although Gq-DREADD is currently one of the most relevant tools available to study astrocyte Gq pathway activation and to modulate astrocyte function, how accurately it reflects Gq pathway activation physiologically *in vivo* remains to be determined.

It was demonstrated that calcium signaling inhibition in hippocampal astrocytes prevented the diversity of neuronal presynaptic strengths (Letellier et al., 2016). Moreover, a study showed that reduction of astrocyte calcium signals in the striatum greatly increased the interneuronal correlation of striatal medium spiny neurons during nongrooming episodes (Yu et al., 2018). Our finding that astrocytic Gq activation and the associated reduction of astrocyte calcium dynamics increase nonencoding neuronal correlations is consistent with these findings. Together, they support a role for astrocytes in the maintenance of neuronal decorrelation and synaptic strength heterogeneity.

Finally, RNAseq of wild-type astrocytes in response to motor learning showed changes in expression for a small number of individual genes and for a larger number of gene sets, which more directly implicates astrocytes in the acquisition of learned behavior. In particular, glutamate transport stood out from the identified enriched gene sets, supporting our interpretation of the functional data that astrocyte glutamate transport contributes to neuronal plasticity M1 during motor learning. These results suggest that astrocytes display plasticity at the gene expression level, which then likely contributes to functional plasticity in both astrocytes and neurons associated with motor learning. Our findings also point to potential mechanisms by which astrocyte manipulations disrupt astrocyte-neuron plasticity during learning. We observed that decreased astrocyte GLT1 levels and activation of astrocyte Gq signaling both prevented a number of gene expression changes during motor learning and also revealed that activation of astrocyte Gq signaling triggered an increase in *Slc1a2*/GLT1 expression. Gq activation thus may be expected to have contrasting effects compared with GLT1 inhibition in M1 astrocytes. Although some effects were symmetrically opposed, others were not, suggesting a complex relationship between function and calcium activity in astrocytes. Our profiling of transcriptomic changes also highlighted other enriched gene sets, particularly GABA and taurine transporters, and differentially expressed genes including extracellular matrix proteins, likely to be functionally relevant to the contributions of M1 astrocytes during motor learning.

Together, our study confirms that astrocytes contribute to neuronal activity and plasticity during learning by characterizing two key aspects of astrocyte function. Furthermore, our results show that specific perturbations of astrocyte function affect how neurons carry information during learning, disrupting critical features of neuronal function that drive learned behaviors.

References

Ackerman SD, Perez-Catalan NA, Freeman MR, Doe CQ (2021) Astrocytes close a motor circuit critical period. Nature 592:414–420.

Adamsky A, Kol A, Kreisel T, Doron A, Ozeri-Engelhard N, Melcer T, Refaeli R, Horn H, Regev L, Groysman M, London M, Goshen I (2018) Astrocytic activation generates de novo neuronal potentiation and memory enhancement. Cell 174:59–71.e14.

Agarwal A, Wu PH, Hughes EG, Fukaya M, Tischfield MA, Langseth AJ, Wirtz D, Bergles DE (2017) Transient opening of the mitochondrial permeability transition pore induces microdomain calcium transients in astrocyte processes. Neuron 93:587–605.e7.

Agulhon C, Boyt KM, Xie AX, Friocourt F, Roth BL, McCarthy KD (2013) Modulation of the autonomic nervous system and behaviour by acute glial cell Gq protein-coupled receptor activation in vivo. J Physiol 591:5599–5609.

Aida T, Yoshida J, Nomura M, Tanimura A, Iino Y, Soma M, Bai N, Ito Y, Cui W, Aizawa H, Yanagisawa M, Nagai T, Takata N, Tanaka KF, Takayanagi R, Kano M, Götz M, Hirase H, Tanaka K (2015) Astroglial glutamate transporter deficiency increases synaptic excitability and leads to pathological repetitive behaviors in mice. Neuropsychopharmacology 40:1569–1579.

Araque A, Parpura V, Sanzgiri RP, Haydon PG (1999) Tripartite synapses: glia, the unacknowledged partner. Trends Neurosci 22:208–215.

Armbruster BN, Li X, Pausch MH, Herlitze S, Roth BL (2007) Evolving the lock to fit the key to create a family of G protein-coupled receptors potently activated by an inert ligand. Proc Natl Acad Sci U S A 104:5163–5168.

Arnth-Jensen N, Jabaudon D, Scanziani M (2002) Cooperation between independent hippocampal synapses is controlled by glutamate uptake. Nat Neurosci 5:325–331.

Asztely F, Erdemli G, Kullmann DM (1997) Extrasynaptic glutamate spillover in the hippocampus: dependence on temperature and the role of active glutamate uptake. Neuron 18:281–293.

Barnes JR, Mukherjee B, Rogers BC, Nafar F, Gosse M, Parsons MP (2020) The relationship between glutamate dynamics and activity-dependent synaptic plasticity. J Neurosci 40:2793–2807.

Bechtholt-Gompf AJ, Walther HV, Adams MA, Carlezon WA Jr, Ongur D, Cohen BM (2010) Blockade of astrocytic glutamate uptake in rats induces signs of anhedonia and impaired spatial memory. Neuropsychopharmacology 35:2049–2059.

Bergles DE, Diamond JS, Jahr CE (1999) Clearance of glutamate inside the synapse and beyond. Curr Opin Neurobiol 9:293–298.

Cao X, Li LP, Wang Q, Wu Q, Hu HH, Zhang M, Fang YY, Zhang J, Li SJ, Xiong WC, Yan HC, Gao YB, Liu JH, Li XW, Sun LR, Zeng YN, Zhu XH, Gao TM (2013) Astrocyte-derived ATP modulates depressive-like behaviors. Nat Med 19:773–777.

Chai H, Diaz-Castro B, Shigetomi E, Monte E, Octeau JC, Yu X, Cohn W, Rajendran PS, Vondriska TM, Whitelegge JP, Coppola G, Khakh BS (2017) Neural circuit-specialized astrocytes: transcriptomic, proteomic, morphological, and functional evidence. Neuron 95:531–549.e9.

Chen J, Sugihara H, Kim J, Fu Z, Barak B, Sur M, Feng G, Han W (2016) Direct modulation of GFAP-expressing glia in the arcuate nucleus bidirectionally regulates feeding. Elife 5:e18716.

Chen SX, Kim AN, Peters AJ, Komiyama T (2015) Subtype-specific plasticity of inhibitory circuits in motor cortex during motor learning. Nat Neurosci 18:1109–1115.

Cichon J, Gan WB (2015) Branch-specific dendritic Ca(2+) spikes cause persistent synaptic plasticity. Nature 520:180–185.

Clapham DE (2007) Calcium signaling. Cell 131:1047–1058.

Corkrum M, Covelo A, Lines J, Bellocchio L, Pisansky M, Loke K, Quintana R, Rothwell PE, Lujan R, Marsicano G, Martin ED, Thomas MJ, Kofuji P, Araque A (2020) Dopamine-evoked synaptic regulation in the nucleus accumbens requires astrocyte activity. Neuron 105:1036–1047.e5.

Cui W, Mizukami H, Yanagisawa M, Aida T, Nomura M, Isomura Y, Takayanagi R, Ozawa K, Tanaka K, Aizawa H (2014) Glial dysfunction in the mouse habenula causes depressive-like behaviors and sleep disturbance. J Neurosci 34:16273–16285.

Diamond JS, Jahr CE (1997) Transporters buffer synaptically released glutamate on a submillisecond time scale. J Neurosci 17:4672–4687.

Dombeck DA, Graziano MS, Tank DW (2009) Functional clustering of neurons in motor cortex determined by cellular resolution imaging in awake behaving mice. J Neurosci 29:13751–13760.

Doron G, Brecht M (2015) What single-cell stimulation has told us about neural coding. Philos Trans R Soc Lond B Biol Sci 370:20140204.

Durkee CA, Araque A (2019) Diversity and specificity of astrocyte-neuron communication. Neuroscience 396:73–78.

Elsayed GF, Lara AH, Kaufman MT, Churchland MM, Cunningham JP (2016) Reorganization between preparatory and movement population responses in motor cortex. Nat Commun 7:13239.

Engelhard B, Finkelstein J, Cox J, Fleming W, Jang HJ, Ornelas S, Koay SA, Thiberge SY, Daw ND, Tank DW, Witten IB (2019) Specialized coding of sensory, motor and cognitive variables in VTA dopamine neurons. Nature 570:509–513.

Farhy-Tselnicker I, Boisvert MM, Liu H, Dowling C, Erikson GA, Blanco-Suarez E, Farhy C, Shokhirev MN, Ecker JR, Allen NJ (2021) Activity-dependent modulation of synapse-regulating genes in astrocytes. Elife 10:e70514.

Filosa A, Paixão S, Honsek SD, Carmona MA, Becker L, Feddersen B, Gaitanos L, Rudhard Y, Schoepfer R, Klopstock T, Kullander K, Rose CR, Pasquale EB, Klein R (2009) Neuron-glia communication via EphA4/ephrin-A3 modulates LTP through glial glutamate transport. Nat Neurosci 12:1285–1292.

Georgopoulos AP, Schwartz AB, Kettner RE (1986) Neuronal population coding of movement direction. Science 233:1416–1419.

Gloor C, Luft AR, Hosp JA (2015) Biphasic plasticity of dendritic fields in layer V motor neurons in response to motor learning. Neurobiol Learn Mem 125:189–194.

Gomez JA, Perkins JM, Beaudoin GM, Cook NB, Quraishi SA, Szoeke EA, Thangamani K, Tschumi CW, Wanat MJ, Maroof AM, Beckstead MJ, Rosenberg PA, Paladini CA (2019) Ventral tegmental area astrocytes orchestrate avoidance and approach behavior. Nat Commun 10:1455.

Harrison TC, Ayling OG, Murphy TH (2012) Distinct cortical circuit mechanisms for complex forelimb movement and motor map topography. Neuron 74:397–409.

Hasel P, Dando O, Jiwaji Z, Baxter P, Todd AC, Heron S, Márkus NM, McQueen J, Hampton DW, Torvell M, Tiwari SS, McKay S, Eraso-Pichot A, Zorzano A, Masgrau R, Galea E, Chandran S, Wyllie DJA, Simpson TI, Hardingham GE (2017) Neurons and neuronal activity control gene expression in astrocytes to regulate their development and metabolism. Nat Commun 8:15132.

Haydon PG (2001) GLIA: listening and talking to the synapse. Nat Rev Neurosci 2:185–193.

Henneberger C, Papouin T, Oliet SH, Rusakov DA (2010) Long-term potentiation depends on release of D-serine from astrocytes. Nature 463:232–236.

Hennes M, Lombaert N, Wahis J, Van den Haute C, Holt MG, Arckens L (2020) Astrocytes shape the plastic response of adult cortical neurons to vision loss. Glia 68:2102–2118.

Hira R, Ohkubo F, Ozawa K, Isomura Y, Kitamura K, Kano M, Kasai H, Matsuzaki M (2013) Spatiotemporal dynamics of functional clusters of neurons in the mouse motor cortex during a voluntary movement. J Neurosci 33:1377–1390.

Holt LM, Olsen ML (2016) Novel applications of magnetic cell sorting to analyze cell-type specific gene and protein expression in the central nervous system. PLoS One 11:e0150290.

Hoshiba Y, Wada T, Hayashi-Takagi A (2017) Synaptic ensemble underlying the selection and consolidation of neuronal circuits during learning. Front Neural Circuits 11:12.

Hösli L, Binini N, Ferrari KD, Thieren L, Looser ZJ, Zuend M, Zanker HS, Berry S, Holub M, Möbius W, Ruhwedel T, Nave KA, Giaume C, Weber B, Saab AS (2022) Decoupling astrocytes in adult mice impairs synaptic plasticity and spatial learning. Cell Rep 38:110484.

Huang L, Ledochowitsch P, Knoblich U, Lecoq J, Murphy GJ, Reid RC, de Vries SE, Koch C, Zeng H, Buice MA, Waters J, Li L (2021) Relationship between simultaneously recorded spiking activity and fluorescence signal in GCaMP6 transgenic mice. Elife 10:e51675.

Huang YH, Sinha SR, Tanaka K, Rothstein JD, Bergles DE (2004) Astrocyte glutamate transporters regulate metabotropic glutamate receptor-mediated excitation of hippocampal interneurons. J Neurosci 24:4551–4559.

Iwai Y, Ozawa K, Yahagi K, Mishima T, Akther S, Vo CT, Lee AB, Tanaka M, Itohara S, Hirase H (2021) Transient astrocytic Gq signaling underlies remote memory enhancement. Front Neural Circuits 15:658343.

John CS, Smith KL, Van't Veer A, Gompf HS, Carlezon WA Jr, Cohen BM, Ongur D, Bechtholt-Gompf AJ (2012) Blockade of astrocytic

glutamate uptake in the prefrontal cortex induces anhedonia. Neuropsychopharmacology 37:2467–2475.

Katagiri H, Tanaka K, Manabe T (2001) Requirement of appropriate glutamate concentrations in the synaptic cleft for hippocampal LTP induction. Eur J Neurosci 14:547–553.

Kawai R, Markman T, Poddar R, Ko R, Fantana AL, Dhawale AK, Kampff AR, Ölveczky BP (2015) Motor cortex is required for learning but not for executing a motor skill. Neuron 86:800–812.

Khakh BS, Sofroniew MV (2015) Diversity of astrocyte functions and phenotypes in neural circuits. Nat Neurosci 18:942–952.

Kim JH, Rahman MH, Lee WH, Suk K (2021) Chemogenetic stimulation of the G(i) pathway in astrocytes suppresses neuroinflammation. Pharmacol Res Perspect 9:e00822.

Kofuji P, Araque A (2021) G-protein-coupled receptors in astrocyte-neuron communication. Neuroscience 456:71–84.

Kol A, Adamsky A, Groysman M, Kreisel T, London M, Goshen I (2020) Astrocytes contribute to remote memory formation by modulating hippocampal-cortical communication during learning. Nat Neurosci 23:1229–1239.

Letellier M, Park YK, Chater TE, Chipman PH, Gautam SG, Oshima-Takago T, Goda Y (2016) Astrocytes regulate heterogeneity of presynaptic strengths in hippocampal networks. Proc Natl Acad Sci U S A 113: E2685–2694.

Lines J, Martin ED, Kofuji P, Aguilar J, Araque A (2020) Astrocytes modulate sensory-evoked neuronal network activity. Nat Commun 11:3689.

Martin-Fernandez M, Jamison S, Robin LM, Zhao Z, Martin ED, Aguilar J, Benneyworth MA, Marsicano G, Araque A (2017) Synapse-specific astrocyte gating of amygdala-related behavior. Nat Neurosci 20:1540–1548.

Mederos S, Hernandez-Vivanco A, Ramirez-Franco J, Martin-Fernandez M, Navarrete M, Yang A, Boyden ES, Perea G (2019) Melanopsin for precise optogenetic activation of astrocyte-neuron networks. Glia 67:915–934.

Mi H, Muruganujan A, Huang X, Ebert D, Mills C, Guo X, Thomas PD (2019) Protocol update for large-scale genome and gene function analysis with the PANTHER classification system (v.14.0). Nat Protoc 14:703–721.

Mizuno N, Itoh H (2009) Functions and regulatory mechanisms of Gq-signaling pathways. Neurosignals 17:42–54.

Murphy-Royal C, Dupuis JP, Varela JA, Panatier A, Pinson B, Baufreton J, Groc L, Oliet SH (2015) Surface diffusion of astrocytic glutamate transporters shapes synaptic transmission. Nat Neurosci 18:219–226.

Murphy-Royal C, Dupuis J, Groc L, Oliet SHR (2017) Astroglial glutamate transporters in the brain: regulating neurotransmitter homeostasis and synaptic transmission. J Neurosci Res 95:2140–2151.

Musall S, Kaufman MT, Juavinett AL, Gluf S, Churchland AK (2019) Single-trial neural dynamics are dominated by richly varied movements. Nat Neurosci 22:1677–1686.

Nagai J, Rajbhandari AK, Gangwani MR, Hachisuka A, Coppola G, Masmanidis SC, Fanselow MS, Khakh BS (2019) Hyperactivity with disrupted attention by activation of an astrocyte synaptogenic cue. Cell 177:1280–1292.e20.

Nagai J, Bellafard A, Qu Z, Yu X, Ollivier M, Gangwani MR, Diaz-Castro B, Coppola G, Schumacher SM, Golshani P, Gradinaru V, Khakh BS (2021) Specific and behaviorally consequential astrocyte G(q) GPCR signaling attenuation in vivo with ibetaARK. Neuron 109:2256–2274.

Niederberger E, Schmidtko A, Rothstein JD, Geisslinger G, Tegeder I (2003) Modulation of spinal nociceptive processing through the glutamate transporter GLT-1. Neuroscience 116:81–87.

Nudo RJ, Milliken GW, Jenkins WM, Merzenich MM (1996) Use-dependent alterations of movement representations in primary motor cortex of adult squirrel monkeys. J Neurosci 16:785–807.

Oliet SH, Piet R, Poulain DA (2001) Control of glutamate clearance and synaptic efficacy by glial coverage of neurons. Science 292:923–926.

Oliveira JF, Sardinha VM, Guerra-Gomes S, Araque A, Sousa N (2015) Do stars govern our actions? Astrocyte involvement in rodent behavior. Trends Neurosci 38:535–549.

Omrani A, Melone M, Bellesi M, Safiulina V, Aida T, Tanaka K, Cherubini E, Conti F (2009) Up-regulation of GLT-1 severely impairs LTD at mossy fibre–CA3 synapses. J Physiol 587:4575–4588.

Pachitariu M, Stringer C, Dipoppa M, Schröder S, Rossi LF, Dalgleish H, Carandini M, Harris KD (2017) Suite2p: beyond 10,000 neurons with standard two-photon microscopy. bioRxiv 061507. https://doi.org/10.1101/061507.

Padmashri R, Suresh A, Boska MD, Dunaevsky A (2015) Motor-skill learning is dependent on astrocytic activity. Neural Plast 2015:938023.

Pannasch U, Vargová L, Reingruber J, Ezan P, Holcman D, Giaume C, Syková E, Rouach N (2011) Astroglial networks scale synaptic activity and plasticity. Proc Natl Acad Sci U S A 108:8467–8472.

Pardo AC, Wong V, Benson LM, Dykes M, Tanaka K, Rothstein JD, Maragakis NJ (2006) Loss of the astrocyte glutamate transporter GLT1 modifies disease in SOD1(G93A) mice. Exp Neurol 201:120–130.

Perea G, Sur M, Araque A (2014a) Neuron-glia networks: integral gear of brain function. Front Cell Neurosci 8:378.

Perea G, Yang A, Boyden ES, Sur M (2014b) Optogenetic astrocyte activation modulates response selectivity of visual cortex neurons in vivo. Nat Commun 5:3262.

Peters AJ, Chen SX, Komiyama T (2014) Emergence of reproducible spatio-temporal activity during motor learning. Nature 510:263–267.

Peters AJ, Liu H, Komiyama T (2017) Learning in the rodent motor cortex. Annu Rev Neurosci 40:77–97.

Porter JT, McCarthy KD (1997) Astrocytic neurotransmitter receptors in situ and in vivo. Prog Neurobiol 51:439–455.

Poskanzer KE, Yuste R (2016) Astrocytes regulate cortical state switching in vivo. Proc Natl Acad Sci U S A 113:E2675-2684

Ribot J, Breton R, Calvo CF, Moulard J, Ezan P, Zapata J, Samama K, Moreau M, Bemelmans AP, Sabatet V, Dingli F, Loew D, Milleret C, Billuart P, Dallerac G, Rouach N (2021) Astrocytes close the mouse critical period for visual plasticity. Science 373:77–81.

Risso D, Schwartz K, Sherlock G, Dudoit S (2011) GC-content normalization for RNA-seq data. BMC Bioinformatics 12:480.

Risso D, Ngai J, Speed TP, Dudoit S (2014) Normalization of RNA-seq data using factor analysis of control genes or samples. Nat Biotechnol 32:896–902.

Robinson MD, McCarthy DJ, Smyth GK (2010) edgeR: a Bioconductor package for differential expression analysis of digital gene expression data. Bioinformatics 26:139–140.

Roth BL (2016) DREADDs for neuroscientists. Neuron 89:683–694.

Rothstein JD, Martin L, Levey AI, Dykes-Hoberg M, Jin L, Wu LD, Nash N, Kuncl RW (1994) Localization of neuronal and glial glutamate transporters. Neuron 13:713–725.

Rothstein JD, Dykes-Hoberg M, Pardo CA, Bristol LA, Jin L, Kuncl RW, Kanai Y, Hediger MA, Wang Y, Schielke JP, Welty DF (1996) Knockout of glutamate transporters reveals a major role for astroglial transport in excitotoxicity and clearance of glutamate. Neuron 16:675–686.

Sasaki T, Ishikawa T, Abe R, Nakayama R, Asada A, Matsuki N, Ikegaya Y (2014) Astrocyte calcium signalling orchestrates neuronal synchronization in organotypic hippocampal slices. J Physiol 592:2771–2783.

Scofield MD, Boger HA, Smith RJ, Li H, Haydon PG, Kalivas PW (2015) Gq-DREADD selectively initiates glial glutamate release and inhibits cue-induced cocaine seeking. Biol Psychiatry 78:441–451.

Suzuki A, Stern SA, Bozdagi O, Huntley GW, Walker RH, Magistretti PJ, Alberini CM (2011) Astrocyte-neuron lactate transport is required for long-term memory formation. Cell 144:810–823.

Takayasu Y, Iino M, Shimamoto K, Tanaka K, Ozawa S (2006) Glial glutamate transporters maintain one-to-one relationship at the climbing fiber-Purkinje cell synapse by preventing glutamate spillover. J Neurosci 26:6563–6572.

Tanaka K, Watase K, Manabe T, Yamada K, Watanabe M, Takahashi K, Iwama H, Nishikawa T, Ichihara N, Kikuchi T, Okuyama S, Kawashima N, Hori S, Takimoto M, Wada K (1997) Epilepsy and exacerbation of brain injury in mice lacking the glutamate transporter GLT-1. Science 276:1699–1702.

Tennant KA, Adkins DL, Donlan NA, Asay AL, Thomas N, Kleim JA, Jones TA (2011) The organization of the forelimb representation of the C57BL/6 mouse motor cortex as defined by intracortical microstimulation and cytoarchitecture. Cereb Cortex 21:865–876.

Trapnell C, Roberts A, Goff L, Pertea G, Kim D, Kelley DR, Pimentel H, Salzberg SL, Rinn JL, Pachter L (2012) Differential gene and transcript expression analysis of RNA-seq experiments with TopHat and Cufflinks. Nat Protoc 7:562–578.

Tsukada S, Iino M, Takayasu Y, Shimamoto K, Ozawa S (2005) Effects of a novel glutamate transporter blocker, (2S, 3S)-3-[3-[4-(trifluoromethyl) benzoylamino]benzyloxy]aspartate (TFB-TBOA), on activities of hippocampal neurons. Neuropharmacology 48:479–491.

Tsvetkov E, Shin RM, Bolshakov VY (2004) Glutamate uptake determines pathway specificity of long-term potentiation in the neural circuitry of fear conditioning. Neuron 41:139–151.

Tzingounis AV, Wadiche JI (2007) Glutamate transporters: confining runaway excitation by shaping synaptic transmission. Nat Rev Neurosci 8:935–947.

Vaidyanathan TV, Collard M, Yokoyama S, Reitman ME, Poskanzer KE (2021) Cortical astrocytes independently regulate sleep depth and duration via separate GPCR pathways. Elife 10:e63329.

Valtcheva S, Venance L (2019) Control of long-term plasticity by glutamate transporters. Front Synaptic Neurosci 11:10.

Verkhratsky A, Nedergaard M (2018) Physiology of astroglia. Physiol Rev 98:239–389.

Ver Steeg G, Galstyan A (2013) Information-theoretic measures of influence based on content dynamics. arXiv:1208.4475v4.

Vogelstein JT, Packer AM, Machado TA, Sippy T, Babadi B, Yuste R, Paninski L (2010) Fast nonnegative deconvolution for spike train inference from population calcium imaging. J Neurophysiol 104:3691–3704.

Wei Z, Lin BJ, Chen TW, Daie K, Svoboda K, Druckmann S (2020) A comparison of neuronal population dynamics measured with calcium imaging and electrophysiology. PLoS Comput Biol 16:e1008198.

Wu D, Smyth GK (2012) Camera: a competitive gene set test accounting for inter-gene correlation. Nucleic Acids Res 40:e133.

Yu X, Taylor AMW, Nagai J, Golshani P, Evans CJ, Coppola G, Khakh BS (2018) Reducing astrocyte calcium signaling *in vivo* alters striatal microcircuits and causes repetitive behavior. Neuron 99:1170–1187.e9.

Zhou Z, Okamoto K, Onodera J, Hiragi T, Andoh M, Ikawa M, Tanaka KF, Ikegaya Y, Koyama R (2021) Astrocytic cAMP modulates memory via synaptic plasticity. Proc Natl Acad Sci U S A 118:e2016584118.